



A discrete-to-continuum model of weakly interacting incommensurate two-dimensional lattices: The hexagonal case

Malena I. Español^a, Dmitry Golovaty^b, J. Patrick Wilber^{b,*}

^a School of Mathematical and Statistical Sciences, Arizona State University, Tempe, AZ 85281, USA

^b Department of Mathematics, University of Akron, Akron, OH 44325, USA



ARTICLE INFO

Keywords:

Heterostructure
Bilayer graphene
Domain wall
Moiré pattern
Discrete-to-continuum modeling

ABSTRACT

In this paper, we extend the discrete-to-continuum procedure we developed in Español et al. (2018) to derive a continuum variational model for a hexagonal twisted bilayer material in which one layer is fixed. We use a discrete energy containing elastic terms and a weak interaction term that could utilize either a Lennard-Jones potential or a Kolmogorov-Crespi potential. To validate our modeling, we perform numerical simulations to compare the predictions of the original discrete model and the proposed continuum model, which also show an agreement with experimental findings for, e.g., twisted bilayer graphene.

1. Introduction

In this paper, we apply a discrete-to-continuum procedure to develop a model that predicts relaxation in a twisted bilayer of hexagonal atomic lattices. Relaxation of bilayer graphene, other layered two-dimensional materials, and van der Waals heterostructures has attracted significant interest over the last several years (Andrei and MacDonald, 2020; Sunku et al., 2018; Carr et al., 2020). Predicting lattice reconstruction and equilibrium configurations is crucial for understanding some of the fundamental physical phenomena displayed by bilayers and heterostructures (Carr et al., 2018, 2019; Cazeaux et al., 2020; Zhang and Tadmor, 2018; Weston et al., 2020). The quasiperiodic relaxed moiré patterns that occur in slightly misaligned or slightly incommensurate lattices induce superlattice effects, which include superconductivity, strong interactions, and other novel electronic and optical properties (Cao et al., 2018; Yoo et al., 2019; Li et al., 2021; Dong et al., 2021). More generally, the study of the mechanics of these nanoscale structures is driven in part by the possibility of engineering advanced materials with novel properties by stacking the same or different types of individual layers in appropriate sequences (Novoselov et al., 2016; Sulleiro et al., 0000; Xiang et al., 2020; Tran et al., 2019).

Relaxation can be understood by considering a bilayer of graphene in which the two layers are given an initial small relative rotation. Variations in the local stacking between the layers generate a quasiperiodic moiré pattern with a period that scales inversely with the size of the angle of the relative rotation (see Fig. 1.1). Mechanically, the bilayer has strong intralayer bonding and weak van der Waals interactions between the layers. As a consequence, the atoms in each lattice adjust through in-plane and out-of-plane deformations. As the lattice structure relaxes, local regions with the energetically favorable AB or BA alignment grow, while regions with AA alignment decrease in size. Typically, the relaxed structure exhibits a network of narrow ridges or wrinkles forming domain walls that separate the relatively large commensurate regions with AB and BA stacking between the lattices (van Wijk et al., 2015, 2014; Nam and Koshino, 2017; Jain et al., 2016; Enaldiev et al., 2020).

* Corresponding author.

E-mail address: jw50@uakron.edu (J.P. Wilber).

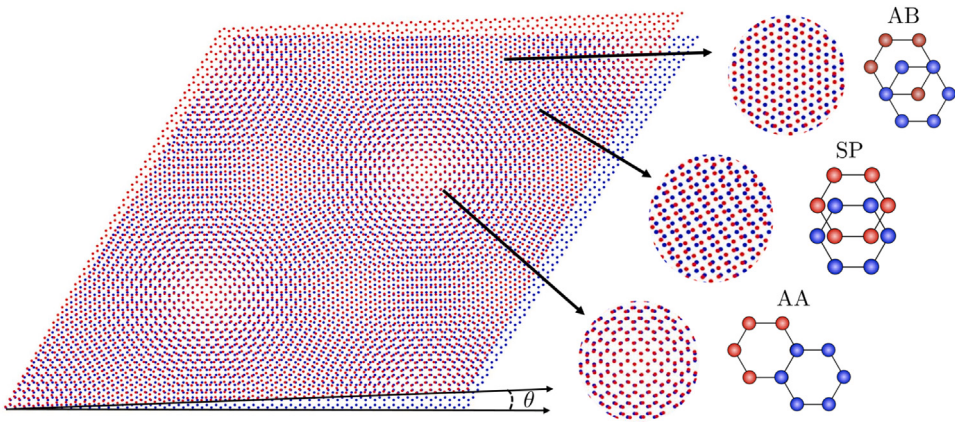


Fig. 1.1. A moiré pattern formed by bilayer graphene with a twist of angle θ , containing three main stacking configurations: AA, AB, and SP.

We derive our continuum model starting from an expression for the discrete energy for two interacting hexagonal lattices. The lattices may have different lattice parameters and there may be a slight relative rotation between the lattices. For simplicity, we keep the atoms on one lattice fixed. In our discrete energy, we model intralayer interactions between neighboring atoms on the deformable lattice with extensional, torsional, and dihedral springs. These describe how the bonds between neighboring atoms resist stretching and bending and how the system maintains an hexagonal lattice structure. The discrete energy also includes a term for the weak interaction between atoms on different lattices. This term is based on a pairwise potential between non-bonded atoms, and we consider both a Lennard-Jones-type potential and a version of the Kolmogorov-Crespi potential (Kolmogorov and Crespi, 2005).

To move from the discrete to the continuum, we introduce a small parameter defined as the ratio of the typical interlayer spacing to the lateral extent of the parallel lattices. Exploiting this small parameter, we develop Taylor expansions of the terms in our discrete energy. After appropriately truncating these expansions, a Riemann sum argument is used to replace sums over the lattice with integrals. This procedure yields a continuum energy for the interacting bilayer. The minimizers of this continuum energy represent equilibrium configurations of the deformable lattice. We note that our continuum weak interlayer interaction energy is a version of the generalized stacking fault energy (Vitek, 1968; Zhou et al., 2015). Although a continuum description, the weak energy retains information about the local mismatch between the original discrete lattices.

We validate the discrete-to-continuum modeling procedure just described through numerical simulations. We use the open-source discrete modeling software LAMMPS (Plimpton, 1995) to simulate the lattice relaxation predicted by the discrete model. Also, we use the multiphysics software COMSOL (com, 0000) to solve numerically the Euler-Lagrange equations derived from the continuum energy. For both the Lennard-Jones and the Kolmogorov-Crespi potentials, we obtain good agreement between the results of the discrete and continuum numerical simulations for several parameter regimes. In particular, we show that our continuum model can reproduce relaxed moiré patterns observed in the simulations based on the discrete model and observed in other studies (van Wijk et al., 2015; Enaldiev et al., 2020). For the Lennard-Jones potential, there is poor agreement with the out-of-plane displacement of the domain walls in some parameter ranges. However, we show that decreasing the well depth of the potential yields a better match between the discrete and continuum. For the Kolmogorov-Crespi potential, we get good agreement between the discrete and the continuum. Our numerical results indicate that this agreement improves as ϵ decreases, as expected. How well our continuum model works depends on the size of the elastic constants. When the elastic constants are relatively small, the solutions to the discrete simulations exhibit small scale spatial oscillations. This suggests that one of the basic assumptions of our discrete-to-continuum modeling procedure—that the atomic lattice can be embedded in a smooth surface—is violated. In this case, we observe poor agreement between the predictions of the discrete and continuum models. On the other hand, when the elastic constants are relatively large, small-scale spatial oscillations do not occur in the discrete solutions. The continuum model in this case predicts solutions that agree well with the solutions predicted by the discrete model.

This paper extends the discrete-to-continuum procedure developed in our previous papers (Español et al., 2017, 2018). In Español et al. (2017), we use a discrete-to-continuum procedure similar to the procedure in this paper to derive a continuum variational model for two chains of atoms with slightly incommensurate lattices. The continuum model recovers both qualitatively and quantitatively the behavior observed in the corresponding discrete model. The numerical solutions for both models demonstrate the presence of large commensurate regions separated by localized incommensurate domain walls. In Español et al. (2018), we develop a continuum variational model for a two-dimensional deformable square lattice of atoms interacting with a two-dimensional rigid square lattice. We use the same discrete-to-continuum procedure as in this paper. The two lattices have slightly different lattice parameters and there is a small relative rotation between them. We show that the continuum model recovers both qualitatively and quantitatively the behavior observed in the corresponding discrete model.

In Dai et al. (2016a,b), the authors present a multiscale model that predicts the deformation of bilayers of graphene and bilayers of other two-dimensional materials. In their model, the total energy of the bilayer has an elastic contribution, associated with the

stretching and bending of the individual layers, and a misfit energy, which describes the van der Waals interactions between the two layers. The misfit energy is defined using the generalized stacking-fault energy for bilayers, which the authors develop in an earlier publication (Zhou et al., 2015) from density-functional theory calculations. The misfit energy is a function of the separation and disregistry between layers. The continuum model we develop in this paper has essential elements in common with the model presented in Dai et al. (2016a,b). Specifically, our model contains terms for the elastic energy of the deformable layer and a term for the van der Waals interactions between the two layers. However, we derive all terms in our continuum energy by upscaling from an atomistic description of the problem. Our upscaling procedure introduces a small parameter that determines the relative size of the various contributions to the continuum energy. Hence, we gain insight into how the balance of these terms produces phenomena like relaxed moiré patterns in interacting bilayers. Furthermore, our modeling sets the stage for additional analysis to rigorously determine the relation between atomistic and continuum descriptions of the problem (Braides et al., 2007; Braides, 2014).

Structural relaxation in twisted graphene bilayers and the associated electron diffraction patterns were studied in Zhang and Tadmor (2018). The authors use multiscale simulations that show that the relaxation exhibits a localized rotation and shrinking of the AA domains. To explain their results theoretically, the authors develop a continuum model that—similar to our work—has a nonlinear elasticity term describing the mechanical response within a graphene layer. Their elastic energy density consists of a Saint Venant-Kirchhoff membrane term and a Helfrich bending term. For the interlayer energy, the authors develop a discrete–continuum approximation based on the Kolmogorov-Crespi potential, one of the potentials we work with in this paper. Unlike in our work, in Zhang and Tadmor (2018) the interlayer energy is calculated in two parts. Locally, the potential is evaluated exactly over a short-range discrete region. Outside this region, a continuum integral approximation is used (Zhang and Tadmor, 2017).

In Carr et al. (2018), the authors study bilayer relaxation by minimizing a total continuum energy over a collection of all possible local atomic environments, which they call configuration space. For the configuration-space approach, every atomic site in the bilayer is associated with a vector that describes the local relative stacking disregistry at that site. This description is similar to our local horizontal mismatch vector, which we define in developing our expression for the interlayer potential. In Cazeaux et al. (2020), these authors extend configuration-space from bilayers to general weakly coupled incommensurate deformable multi-layers. They derive an elastic model for the relaxation of vertical stacks of any number of incommensurate, weakly coupled deformable layers. When specialized to a bilayer heterostructure, the model in Cazeaux et al. (2020) is similar to the continuum model we derive in this paper, although our upscaling approach is different from theirs.

We mention two other recent papers related to our work. In Halbertal et al. (2021), a model similar to that developed in Carr et al. (2018). The focus in Halbertal et al. (2021) is used to describe how the shapes of moiré domains and domain boundaries yield information about the generalized stacking fault energy function at the low twist-angle limit. The authors of Enaldiev et al. (2020), also motivated by the study of lattice reconstruction in twisted bilayers at low twist angles, use density functional theory to develop interpolation formulae for the interlayer adhesion energies of the bilayers. The authors combine the interlayer adhesion energies with elasticity theory, and the resulting model is used to analyze the mesoscale domain structures formed during lattice relaxation.

This paper is organized as follows. In Section 2, we formulate a discrete energy of the system of a graphene sheet over a substrate. In Section 3, we derive a continuum energy that keeps track of the mismatch of the spacing between the atoms on each curve. Section 4 includes numerical results that compare the atomistic model with the continuum model. We summarize in Section 5.

2. Atomistic model

We consider a discrete system that consists of parallel two-dimensional atomic lattices, $\hat{\mathcal{A}}_0$ and $\hat{\mathcal{A}}$, both infinite in extent. The atoms in $\hat{\mathcal{A}}_0$ are fixed and form a flat hexagonal lattice with lattice parameter h_0 . In this work, $\hat{\mathcal{A}}_0$ describes a rigid substrate. The atoms in $\hat{\mathcal{A}}$ can move and each of these atoms interacts with its neighbors within $\hat{\mathcal{A}}$ via a strong bond potential. $\hat{\mathcal{A}}$ describes a layer of a two-dimensional material that is nearly inextensible and has a finite resistance to bending. In the absence of interactions with atoms on $\hat{\mathcal{A}}_0$, the atoms in $\hat{\mathcal{A}}$ in equilibrium form a flat hexagonal lattice that has lattice parameter h . All atoms in $\hat{\mathcal{A}}$ are assumed to interact with all atoms in $\hat{\mathcal{A}}_0$ via a weak interatomic potential. Below we refer to $\hat{\mathcal{A}}_0$ as the rigid lattice and to $\hat{\mathcal{A}}$ as the deformable lattice.

We assume that $\hat{\mathcal{A}}$ deforms periodically and that, in its reference configuration, one periodic cell of $\hat{\mathcal{A}}$ occupies a parallelogram-shaped, planar domain \mathcal{A}^0 with sides of length L . To define \mathcal{A}^0 , we set $\mathbf{a}_1 = (1, 0)$ and $\mathbf{a}_2 = (1/2, \sqrt{3}/2)$ and we define

$$\mathcal{A}^0 = \{(\mathbf{x}, \sigma) : \mathbf{x} = y_1 \mathbf{a}_1 + y_2 \mathbf{a}_2 \text{ with } (y_1, y_2) \in [0, L]^2\}. \quad (2.1)$$

We set $N = L/h$. The set \mathcal{A}^0 can be divided into N^2 unit cells each containing two atoms. See Fig. 2.1. The positions of the atoms in the reference configuration of \mathcal{A}^0 are

$$\mathbf{r}_{ij}^k = (h((i+k/3)\mathbf{a}_1 + (j+k/3)\mathbf{a}_2), \sigma) \text{ for } k = 1, 2 \text{ and } i, j = 1, \dots, N. \quad (2.2)$$

The positions of the atoms in the deformed configuration of \mathcal{A}^0 are

$$\mathbf{q}_{ij}^k = \mathbf{r}_{ij}^k + (\mathbf{u}_{ij}^k, v_{ij}^k) \text{ for } k = 1, 2 \text{ and } i, j = 1, \dots, N, \quad (2.3)$$

where \mathbf{u}_{ij}^k is the displacement in the x, y plane, and v_{ij}^k in the z -direction. Because $\hat{\mathcal{A}}$ deforms periodically, we identify $i = N + 1$ with $i = 1$ and $j = N + 1$ with $j = 1$.

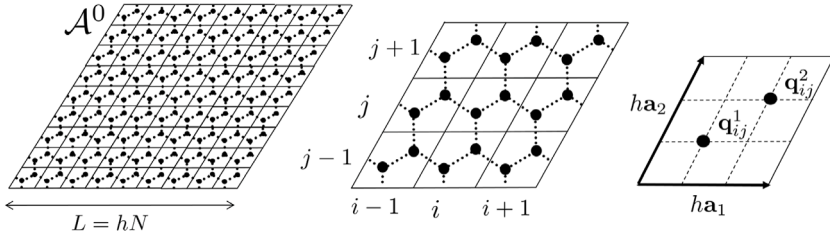


Fig. 2.1. Left: \mathcal{A}^0 consists of N^2 unit cells. Middle: each unit cell is indexed by i, j . Right: the unit cell i, j contains two atoms \mathbf{q}_{ij}^1 and \mathbf{q}_{ij}^2 . The lattice vectors $h\mathbf{a}_1$ and $h\mathbf{a}_2$ are also shown.

For the rigid lattice, the current and the reference configurations are the same. To describe these, we define the rotation matrix

$$R(\theta) = \begin{pmatrix} \cos \theta & -\sin \theta \\ \sin \theta & \cos \theta \end{pmatrix}$$

and we define $\mathbf{a}_i^0 = R(\theta)\mathbf{a}_i$ for $i = 1, 2$. We assume that there is a unit cell of $\hat{\mathcal{A}}$ whose lower left corner sits directly above the lower left corner of a unit cell in $\hat{\mathcal{A}}_0$. Then, the positions of atoms on the rigid lattice are

$$\mathbf{p}_{\ell m}^{\tilde{k}} = (h_0 ((\ell + \tilde{k}/3)\mathbf{a}_1^0 + (m + \tilde{k}/3)\mathbf{a}_2^0), 0) \text{ for } \tilde{k} = 1, 2 \text{ and } \ell, m = 1, \dots, \infty. \quad (2.4)$$

As stated above, we assume that $\hat{\mathcal{A}}$ is infinite in extent and deforms periodically. The size of \mathcal{A}^0 is chosen so that in the discrete simulations we perform to validate the modeling, several periods of the anticipated moiré pattern fit within the computational domain in both directions. Hence this would allow the system the possibility of selecting a larger pattern size. Periodicity was assumed in part to facilitate imposing the same boundary conditions in the discrete and continuum simulations and to avoid boundary effects. Periodicity puts a constraint on the admissible choices of θ , the relative rotation between the lattices in the reference configuration, and h and h_0 , the lattice parameters. The details on how we satisfy this constraint are presented in Section 4.1 below.

Note that in the reference configuration, the lattices are planar, parallel, and separated by a distance σ . Here σ is a length scale associated with the weak potential. When $h_0 = h$ (e.g., bilayer graphene) and $\theta = 0$, the equilibrium configuration of the system $\hat{\mathcal{A}}$ is shifted relatively to $\hat{\mathcal{A}}_0$ such that half of the atoms in $\hat{\mathcal{A}}$ sit above the centers of the hexagons in $\hat{\mathcal{A}}_0$ (AB stacking). The system would be in *global registry*. In this paper, we consider the situation where $\hat{\mathcal{A}}_0$ and $\hat{\mathcal{A}}$ in the reference configuration have slightly different orientations (small values of θ) and/or when they have slightly different lattice parameter ($h_0 \neq h$, but $|h_0 - h|/h_0 \ll 1$). See Fig. 1.1.

We assume that the total energy of the discrete system depends on the position of the atoms in the deformable lattice and is given by

$$E := E_s + E_t + E_d + E_w. \quad (2.5)$$

That is, the total energy is the sum of the intralayer energy—composed of the *stretching* E_s , *torsional* E_t , and *dihedral* E_d energies—and the interlayer (weak) energy E_w .

The stretching energy E_s is the energy associated with stretching or compressing bonds between neighboring atoms in $\hat{\mathcal{A}}$. Using a harmonic potential, we define

$$E_s := \sum_{i,j=1}^N \frac{k_s}{2} \left[\left(\frac{\|\mathbf{b}_{ij}^1\| - \frac{h}{\sqrt{3}}}{\frac{h}{\sqrt{3}}} \right)^2 + \left(\frac{\|\mathbf{b}_{ij}^2\| - \frac{h}{\sqrt{3}}}{\frac{h}{\sqrt{3}}} \right)^2 + \left(\frac{\|\mathbf{b}_{ij}^3\| - \frac{h}{\sqrt{3}}}{\frac{h}{\sqrt{3}}} \right)^2 \right], \quad (2.6)$$

where the vectors

$$\mathbf{b}_{ij}^1 = \mathbf{q}_{ij}^1 - \mathbf{q}_{ij}^2, \quad \mathbf{b}_{ij}^2 = \mathbf{q}_{i+1j}^1 - \mathbf{q}_{ij}^2, \quad \text{and} \quad \mathbf{b}_{ij}^3 = \mathbf{q}_{i+1j}^1 - \mathbf{q}_{ij}^2$$

represent the bonds between the atom \mathbf{q}_{ij}^2 and its neighbors for every unit cell $i, j = 1, \dots, N$ (see Fig. 2.2 (left)). In (2.6), k_s is the spring constant.

The torsional energy is the energy associated with changing the angle between adjacent bonds. We model this energy by assuming we have torsional springs between adjacent bonds. Each atom is related to three torsional springs, and therefore each unit cell contains six torsional springs. The torsional energy is

$$E_t := \sum_{i,j=1}^N \frac{k_t}{2} \left[\left(\phi(\mathbf{b}_{ij}^1, \mathbf{b}_{ij}^2) - 2\pi/3 \right)^2 + \left(\phi(\mathbf{b}_{ij}^2, \mathbf{b}_{ij}^3) - 2\pi/3 \right)^2 + \left(\phi(\mathbf{b}_{ij}^1, \mathbf{b}_{ij}^3) - 2\pi/3 \right)^2 + \left(\phi(-\mathbf{b}_{i-1j}^3, \mathbf{b}_{ij}^1) - 2\pi/3 \right)^2 + \left(\phi(-\mathbf{b}_{ij-1}^2, \mathbf{b}_{ij}^1) - 2\pi/3 \right)^2 + \left(\phi(-\mathbf{b}_{i-1j}^3, \mathbf{b}_{ij-1}^2) - 2\pi/3 \right)^2 \right], \quad (2.7)$$

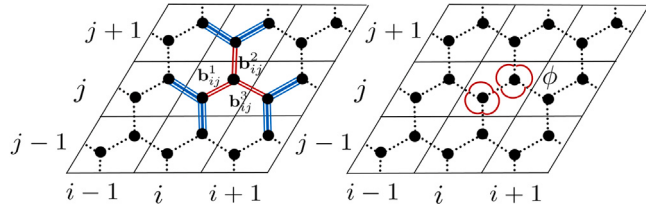


Fig. 2.2. Left: The lattice with the main three bonds (red double lines) corresponding to the i,j unit cell, used to define the stretching energy and the adjacent bonds (blue triple lines) used to defined the dihedral angles. Right: The six angles ϕ (red solid lines) corresponding to the i,j init cell used to define the torsional energy.

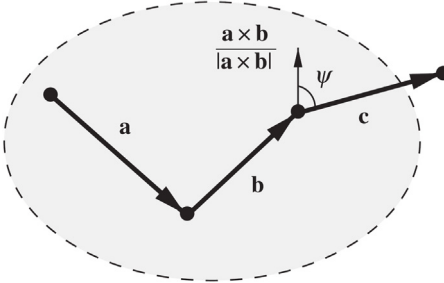


Fig. 2.3. A dihedral spring connecting vectors \mathbf{a} , \mathbf{b} , and \mathbf{c} . The spring energy is minimized when $\psi = \pi/2$.

where k_t is the torsional spring constant and $\phi(\mathbf{a}, \mathbf{c})$ is the angle between the vectors \mathbf{a} and \mathbf{c} . Right of Fig. 2.2 shows the six angles corresponding to the unit cell i,j .

Assuming that admissible in-plane deformations of $\hat{\mathcal{A}}$ are small, we can use the approximation

$$\phi = \arccos(x) \approx \arccos(-1/2) + \frac{1}{\sin(\arccos(-1/2))}(x + 1/2) = \frac{2\pi}{3} + \frac{2}{\sqrt{3}} \left(\cos(\phi) + \frac{1}{2} \right)$$

to rewrite E_t as

$$E_t = \sum_{i,j=1}^N \frac{k_t}{2} \frac{4}{3} \left[\left(\frac{\mathbf{b}_{ij}^1 \cdot \mathbf{b}_{ij}^2}{\|\mathbf{b}_{ij}^1\| \|\mathbf{b}_{ij}^2\|} + \frac{1}{2} \right)^2 + \left(\frac{\mathbf{b}_{ij}^2 \cdot \mathbf{b}_{ij}^3}{\|\mathbf{b}_{ij}^2\| \|\mathbf{b}_{ij}^3\|} + \frac{1}{2} \right)^2 + \left(\frac{\mathbf{b}_{ij}^1 \cdot \mathbf{b}_{ij}^3}{\|\mathbf{b}_{ij}^1\| \|\mathbf{b}_{ij}^3\|} + \frac{1}{2} \right)^2 \right. \\ \left. + \left(\frac{\mathbf{b}_{i-1j}^3 \cdot \mathbf{b}_{ij}^1}{\|\mathbf{b}_{i-1j}^3\| \|\mathbf{b}_{ij}^1\|} + \frac{1}{2} \right)^2 + \left(\frac{\mathbf{b}_{ij-1}^2 \cdot \mathbf{b}_{ij}^1}{\|\mathbf{b}_{ij-1}^2\| \|\mathbf{b}_{ij}^1\|} + \frac{1}{2} \right)^2 + \left(\frac{\mathbf{b}_{i-1j}^3 \cdot \mathbf{b}_{ij-1}^2}{\|\mathbf{b}_{i-1j}^3\| \|\mathbf{b}_{ij-1}^2\|} + \frac{1}{2} \right)^2 \right]. \quad (2.8)$$

Certain out-of-plane deformations are not penalized by the extensional and torsional energies. For example, there is no energy cost for folding along a direction parallel to the sides of \mathcal{A}^0 . To penalize for such deformations, we introduce the dihedral energy by assuming that a dihedral spring connects every triplet of adjacent bonds. This spring energy is minimized when the third bond lies in the plane formed by the first two bonds. See Fig. 2.3. We assume that the energy of a dihedral spring is

$$e_d(\mathbf{a}, \mathbf{b}, \mathbf{c}) := \frac{k_d}{2} \cos^2 \psi = \frac{k_d}{2} \frac{((\mathbf{a} \times \mathbf{b}) \cdot \mathbf{c})^2}{\|\mathbf{a} \times \mathbf{b}\|^2 \|\mathbf{c}\|^2},$$

where k_d is the dihedral spring constant and ψ is the dihedral angle defined as in Fig. 2.3. For each $i, j = 1, \dots, N$, each bond \mathbf{b}_{ij}^p , $p = 1, 2, 3$ is the ‘middle’ bond in four different triplets of adjacent bonds. See Fig. 2.2.

Hence the total dihedral energy is

$$E_d := \sum_{i,j=1}^N \frac{k_d}{2} \left\{ \frac{((\mathbf{b}_{ij}^1 \times \mathbf{b}_{ij}^2) \cdot \mathbf{b}_{ij-1}^2)^2}{\|\mathbf{b}_{ij}^1 \times \mathbf{b}_{ij}^2\|^2 \|\mathbf{b}_{ij-1}^2\|^2} + \frac{((\mathbf{b}_{ij}^1 \times \mathbf{b}_{ij}^2) \cdot \mathbf{b}_{i-1j}^3)^2}{\|\mathbf{b}_{ij}^1 \times \mathbf{b}_{ij}^2\|^2 \|\mathbf{b}_{i-1j}^3\|^2} + \frac{((\mathbf{b}_{ij}^1 \times \mathbf{b}_{ij}^3) \cdot \mathbf{b}_{ij-1}^2)^2}{\|\mathbf{b}_{ij}^1 \times \mathbf{b}_{ij}^3\|^2 \|\mathbf{b}_{ij-1}^2\|^2} + \right. \\ \left. \frac{((\mathbf{b}_{ij}^1 \times \mathbf{b}_{ij}^3) \cdot \mathbf{b}_{i-1j}^3)^2}{\|\mathbf{b}_{ij}^1 \times \mathbf{b}_{ij}^3\|^2 \|\mathbf{b}_{i-1j}^3\|^2} + \frac{((\mathbf{b}_{ij}^2 \times \mathbf{b}_{ij}^3) \cdot \mathbf{b}_{ij}^1)^2}{\|\mathbf{b}_{ij}^2 \times \mathbf{b}_{ij}^3\|^2 \|\mathbf{b}_{ij}^1\|^2} + \frac{((\mathbf{b}_{ij}^2 \times \mathbf{b}_{ij}^3) \cdot \mathbf{b}_{i-1j+1}^1)^2}{\|\mathbf{b}_{ij}^2 \times \mathbf{b}_{ij}^3\|^2 \|\mathbf{b}_{i-1j+1}^1\|^2} + \frac{((\mathbf{b}_{ij}^2 \times \mathbf{b}_{ij}^3) \cdot \mathbf{b}_{ij}^1)^2}{\|\mathbf{b}_{ij}^2 \times \mathbf{b}_{ij}^3\|^2 \|\mathbf{b}_{ij}^1\|^2} + \right. \\ \left. \frac{((\mathbf{b}_{ij}^2 \times \mathbf{b}_{ij}^1) \cdot \mathbf{b}_{ij+1}^1)^2}{\|\mathbf{b}_{ij}^2 \times \mathbf{b}_{ij}^1\|^2 \|\mathbf{b}_{ij+1}^1\|^2} + \frac{((\mathbf{b}_{ij}^2 \times \mathbf{b}_{ij+1}^1) \cdot \mathbf{b}_{ij}^3)^2}{\|\mathbf{b}_{ij}^2 \times \mathbf{b}_{ij+1}^1\|^2 \|\mathbf{b}_{ij}^3\|^2} + \frac{((\mathbf{b}_{ij}^2 \times \mathbf{b}_{ij}^1) \cdot \mathbf{b}_{i+1j}^1)^2}{\|\mathbf{b}_{ij}^2 \times \mathbf{b}_{ij}^1\|^2 \|\mathbf{b}_{i+1j}^1\|^2} + \right. \\ \left. \frac{((\mathbf{b}_{ij}^3 \times \mathbf{b}_{ij}^1) \cdot \mathbf{b}_{ij+1}^1)^2}{\|\mathbf{b}_{ij}^3 \times \mathbf{b}_{ij}^1\|^2 \|\mathbf{b}_{ij+1}^1\|^2} + \frac{((\mathbf{b}_{ij}^3 \times \mathbf{b}_{ij}^1) \cdot \mathbf{b}_{i+1j}^1)^2}{\|\mathbf{b}_{ij}^3 \times \mathbf{b}_{ij}^1\|^2 \|\mathbf{b}_{i+1j}^1\|^2} \right\}$$

$$\left\{ \frac{\left((\mathbf{b}_{ij}^3 \times \mathbf{b}_{ij}^2) \cdot \mathbf{b}_{i+1j-1}^2 \right)^2}{\|\mathbf{b}_{ij}^3 \times \mathbf{b}_{ij}^2\|^2 \|\mathbf{b}_{i+1j-1}^2\|^2} + \frac{\left((\mathbf{b}_{ij}^3 \times \mathbf{b}_{ij}^1) \cdot \mathbf{b}_{i+1j}^1 \right)^2}{\|\mathbf{b}_{ij}^3 \times \mathbf{b}_{ij}^1\|^2 \|\mathbf{b}_{i+1j}^1\|^2} + \frac{\left((\mathbf{b}_{ij}^3 \times \mathbf{b}_{ij}^1) \cdot \mathbf{b}_{i+1j-1}^2 \right)^2}{\|\mathbf{b}_{ij}^3 \times \mathbf{b}_{ij}^1\|^2 \|\mathbf{b}_{i+1j-1}^2\|^2} \right\}. \quad (2.9)$$

The bending between interatomic bonds is penalized by introducing harmonic torsional springs and dihedral angles between the bonds. The expressions for the extensional and torsional springs, respectively, show that the sum of the corresponding energy components is minimized when the atoms on $\hat{\mathcal{A}}$ form a hexagonal lattice with sides of length $h/\sqrt{3}$.

Finally, we consider two choices for the energy of the weak interaction between $\hat{\mathcal{A}}_0$ and $\hat{\mathcal{A}}$. Our first choice is to define

$$E_w = \omega \sum_{i,j=1}^N \sum_{k=1}^2 \sum_{\ell,m=-\infty}^{\infty} \sum_{\tilde{k}=1}^2 g_{\text{LJ}} \left(\frac{\|\mathbf{q}_{ij}^k - \mathbf{p}_{\ell m}^{\tilde{k}}\|}{\sigma} \right), \quad (2.10)$$

where g_{LJ} is the classical Lennard-Jones 12–6 potential

$$g_{\text{LJ}}(r) = r^{-12} - 2r^{-6}. \quad (2.11)$$

The parameters σ and ω define the equilibrium interatomic distance and the strength of the Lennard-Jones potential, respectively. Note that the inner double sum in (2.10) is taken over the entire rigid lattice to properly account for weak interactions between the lattices.

The Lennard-Jones potential fails to adequately account for the registry dependence in the interaction between bilayers. The Kolmogorov–Crespi potential addresses this deficiency (Kolmogorov and Crespi, 2005). Therefore, the second choice we consider for the weak interaction is

$$E_w = \omega \sum_{i,j=1}^N \sum_{k=1}^2 \sum_{\ell,m=-\infty}^{\infty} \sum_{\tilde{k}=1}^2 g_{\text{KC}} \left(\frac{\|\mathbf{q}_{ij}^k - \mathbf{p}_{\ell m}^{\tilde{k}}\|}{\sigma}, \frac{\hat{\rho}(\mathbf{q}_{ij}^k - \mathbf{p}_{\ell m}^{\tilde{k}})}{\bar{\delta}} \right), \quad (2.12)$$

where g_{KC} is a version of the Kolmogorov–Crespi potential having the form

$$g_{\text{KC}}(r, \rho) = e^{-\tilde{\lambda}(r-1)} [\tilde{C} + 2f(\rho)] - r^{-6} \quad \text{with} \quad f(\rho) = e^{-\rho^2} (\tilde{C}_0 + \tilde{C}_2 \rho^2 + \tilde{C}_4 \rho^4). \quad (2.13)$$

In (2.12), $\hat{\rho}(\mathbf{a})$ is the length of the projection of \mathbf{a} onto the xy -plane, which is the plane containing the fixed lattice $\hat{\mathcal{A}}_0$. For g_{KC} , ω can be associated with the strength of the potential. The parameters σ and $\bar{\delta}$ are lengths; σ is related to the equilibrium spacing between the layers. The constants $\tilde{\lambda}$, \tilde{C} , \tilde{C}_0 , \tilde{C}_2 , and \tilde{C}_4 are dimensionless parameters (Kolmogorov and Crespi, 2005).

3. Continuum model

First, we briefly describe the approach we take to derive the continuum model. We assume that the atoms on the deformable lattice $\hat{\mathcal{A}}$ are embedded in a smooth surface and we describe this surface parametrically in terms of the displacement field. Nondimensionalizing the discrete problem introduces a small geometric parameter $\epsilon = \sigma/L$, equal to the ratio of the equilibrium distance of the weak interaction to the length of the side of the domain D . Evaluating the displacements at atomic positions, substituting these into the expression (2.5) for the discrete energy, expanding the result in terms of ϵ , and converting summation into integration, leads to an expansion in terms of ϵ for the continuum energy, written as a functional of the displacement field. We identify the leading-order terms in this expansion, up to the order at which contributions from the extensional, torsional, and dihedral springs, as well as the van der Waals interactions are included. The resulting continuum energy is of Ginzburg–Landau type and contains terms of different powers in ϵ . The minimizers of the continuum energy typically exhibit bulk regions of registry, separated by thin walls where the gradient of the displacement field is large. Thus, within the walls, the contributions from higher-order terms generally cannot be neglected. We choose to cut off the expansion that leads to the continuum energy at the order when all components of the displacement contribute to the energy density inside the walls at leading order. Finally, in the next section, we present the results of simulations confirming that the behavior of minimizers of the continuum energy match that of minimizers of the discrete energy.

We assume that the deformed configuration of a periodic cell of $\hat{\mathcal{A}}$ is embedded in a sufficiently smooth surface $\mathcal{A} = \{(\mathbf{x} + \mathbf{u}(\mathbf{x}), \sigma + v(\mathbf{x})) : (\mathbf{x}, \sigma) \in \mathcal{A}^0\}$, where $(\mathbf{u}(\mathbf{x}), v(\mathbf{x}))$ is the displacement of the point (\mathbf{x}, σ) on \mathcal{A}^0 . Next, we assume $\sigma \ll L$, that is, the length scale associated with the equilibrium spacing between the lattices is much smaller than the lateral extent of a periodic cell of the system. Then, we define $\epsilon = \sigma/L$ and introduce the rescalings

$$\chi = \frac{\mathbf{x}}{L}, \quad \xi = \frac{\mathbf{u}}{\epsilon L}, \quad \eta = \frac{v}{\epsilon L}, \quad \mathcal{E} = \frac{\epsilon E}{\omega}. \quad (3.1)$$

We define the nondimensional parameters

$$\delta_0 = \frac{h_0}{\sigma}, \quad \delta = \frac{h}{\sigma}, \quad \gamma_s = \frac{6\sqrt{3}k_s}{\omega\delta^2}, \quad \gamma_t = \frac{64\sqrt{3}k_t}{\omega\delta^2}, \quad \gamma_d = \frac{\sqrt{3}k_d}{4\omega}. \quad (3.2)$$

The numerical coefficients in the definitions of γ_s , γ_t , and γ_d are explained later. The scaling for the displacements are appropriate for small deformations considered here. With a slight abuse of notation, we now set

$$\mathcal{A}^0 = \{(\chi, \epsilon) : \chi = y_1 \mathbf{a}_1 + y_2 \mathbf{a}_2 \text{ with } (y_1, y_2) \in [0, 1]^2\}, \quad \mathcal{A} = \{(\chi + \epsilon\xi(\chi), \epsilon + \epsilon\eta(\chi)) : (\chi, \epsilon) \in \mathcal{A}^0\}. \quad (3.3)$$

Also, we set $D_1 = \{\chi : (\chi, \varepsilon) \in \mathcal{A}^0\}$. We assume that $\delta_0, \delta = \mathcal{O}(1)$, that is, the lattice parameters for $\hat{\mathcal{A}}_0$ and $\hat{\mathcal{A}}$ are comparable to the distance between $\hat{\mathcal{A}}_0$ and $\hat{\mathcal{A}}$ (and hence both are much smaller than the lateral extent of a periodic cell of the system). Furthermore, in order to observe the registry effects on a macroscale, we assume that

$$\alpha := \frac{\delta_0 - \delta}{\varepsilon \delta} = \mathcal{O}(1), \quad (3.4)$$

so that the mismatch between the equilibrium lattice parameters of $\hat{\mathcal{A}}_0$ and $\hat{\mathcal{A}}$ is small.

In the rescaled coordinates, the atoms on \mathcal{A}^0 are located at the points $\mathbf{r}_{ij}^k = (\chi_{ij}^k, \varepsilon)$, where

$$\chi_{ij}^k = \varepsilon \delta ((i + k/3)\mathbf{a}_1 + (j + k/3)\mathbf{a}_2) \quad (3.5)$$

for $i, j = 1, \dots, N$ and $k = 1, 2$, are obtained by dividing \mathbf{r}_{ij}^k by L in (2.2). Atom k in the i, j unit cell is then displaced to the point

$$\mathbf{q}_{ij}^k = (\chi_{ij}^k + \varepsilon \xi(\chi_{ij}^k), \varepsilon + \varepsilon \eta(\chi_{ij}^k)). \quad (3.6)$$

Note that here and in what follows we continue to use the notation \mathbf{q}_{ij}^k , \mathbf{r}_{ij}^k , and \mathbf{b}_{ij}^p , but now to denote the corresponding nondimensional quantities.

3.1. Elastic energy contribution

The developments in this section closely follow those in Español et al. (2018). Using that ε is small, we Taylor expand the rescaled versions of the components (2.6), (2.9), and (2.9) of the discrete elastic energy in ε about $\xi(\chi_{ij}^2)$. After truncating the expansions, we end up with approximate energies as a function of ξ and η evaluated at χ_{ij}^2 , where $i, j = 1, \dots, N$. The details of the derivations that led to these truncated expansions and the definitions of \mathbf{v}_1 , \mathbf{v}_2 , and \mathbf{v}_3 are given in the Supplementary Material. This yields

$$\begin{aligned} \mathcal{E}_s[\xi, \eta] &\approx \sum_{i,j=1}^N \frac{9k_s \varepsilon^3}{2\omega} \left[\left(\mathbf{v}_1 \cdot \nabla \xi \mathbf{v}_1 + \frac{\varepsilon}{2} \mathbf{v}_1 \cdot (\nabla \eta \otimes \nabla \eta) \mathbf{v}_1 \right)^2 \right. \\ &\quad + \left(\mathbf{v}_2 \cdot \nabla \xi \mathbf{v}_2 + \frac{\varepsilon}{2} \mathbf{v}_2 \cdot (\nabla \eta \otimes \nabla \eta) \mathbf{v}_2 \right)^2 \\ &\quad \left. + \left(\mathbf{v}_3 \cdot \nabla \xi \mathbf{v}_3 + \frac{\varepsilon}{2} \mathbf{v}_3 \cdot (\nabla \eta \otimes \nabla \eta) \mathbf{v}_3 \right)^2 \right], \end{aligned} \quad (3.7)$$

$$\begin{aligned} \mathcal{E}_t[\xi, \eta] &\approx \sum_{i,j=1}^N \frac{48k_t \varepsilon^3}{\omega} \left[\left(\frac{\mathbf{v}_1 \cdot \nabla \xi \mathbf{v}_2 + \mathbf{v}_2 \cdot \nabla \xi \mathbf{v}_1}{2} + \frac{\varepsilon}{2} (\mathbf{v}_1 \cdot (\nabla \eta \otimes \nabla \eta) \mathbf{v}_2) \right)^2 \right. \\ &\quad + \left(\frac{\mathbf{v}_2 \cdot \nabla \xi \mathbf{v}_3 + \mathbf{v}_3 \cdot \nabla \xi \mathbf{v}_2}{2} + \frac{\varepsilon}{2} (\mathbf{v}_2 \cdot (\nabla \eta \otimes \nabla \eta) \mathbf{v}_3) \right)^2 \\ &\quad \left. + \left(\frac{\mathbf{v}_1 \cdot \nabla \xi \mathbf{v}_3 + \mathbf{v}_3 \cdot \nabla \xi \mathbf{v}_1}{2} + \frac{\varepsilon}{2} (\mathbf{v}_1 \cdot (\nabla \eta \otimes \nabla \eta) \mathbf{v}_3) \right)^2 \right], \end{aligned} \quad (3.8)$$

and

$$\mathcal{E}_d[\xi, \eta] \approx \sum_{i,j=1}^N \frac{3k_d \delta^2 \varepsilon^5}{8\omega} \left[7\eta_{,11}^2 + 16\eta_{,12}^2 - 2\eta_{,11}\eta_{,22} + 7\eta_{,22}^2 \right]. \quad (3.9)$$

As we did in Español et al. (2018), we neglect some third-order terms in ε , in particular, the terms that contain second-order derivatives in ξ or are cubic in derivatives of ξ . Further, we include some quartic terms in the derivative of η , that allow us to complete squares in (3.7) and (3.8). We showed in Español et al. (2018) that including/deleting these higher order terms from the truncated energy gives minimizers with the structure close to that of the minimizers of the discrete energy as $\varepsilon \rightarrow 0$.

We now observe that \mathcal{A}^0 has area $\sqrt{3}/2$ in nondimensional coordinates and that the spacing between the atoms is $\varepsilon \delta / \sqrt{3} \ll 1$. Hence, the number of atoms on \mathcal{A}^0 is $\approx \frac{1}{\varepsilon^2}$. These observations justify replacing the sums in (3.7), (3.8), and (3.9) with integrals to define the continuum elastic energies

$$\mathcal{F}_s^\varepsilon[\xi, \eta] =: \frac{\gamma_s \varepsilon}{2} \int_{D_1} \left[\left(\mathbf{v}_1 \cdot \nabla \xi \mathbf{v}_1 + \frac{\varepsilon}{2} |\nabla \eta \cdot \mathbf{v}_1|^2 \right)^2 + \left(\mathbf{v}_2 \cdot \nabla \xi \mathbf{v}_2 + \frac{\varepsilon}{2} |\nabla \eta \cdot \mathbf{v}_2|^2 \right)^2 + \left(\mathbf{v}_3 \cdot \nabla \xi \mathbf{v}_3 + \frac{\varepsilon}{2} |\nabla \eta \cdot \mathbf{v}_3|^2 \right)^2 \right] d\chi, \quad (3.10)$$

$$\begin{aligned} \mathcal{F}_t^\varepsilon[\xi, \eta] &=: \gamma_t \varepsilon \int_{D_1} \left[\left(\frac{\mathbf{v}_1 \cdot \nabla \xi \mathbf{v}_2 + \mathbf{v}_2 \cdot \nabla \xi \mathbf{v}_1}{2} + \frac{\varepsilon}{2} (\mathbf{v}_1 \cdot (\nabla \eta \otimes \nabla \eta) \mathbf{v}_2) \right)^2 \right. \\ &\quad + \left(\frac{\mathbf{v}_2 \cdot \nabla \xi \mathbf{v}_3 + \mathbf{v}_3 \cdot \nabla \xi \mathbf{v}_2}{2} + \frac{\varepsilon}{2} (\mathbf{v}_2 \cdot (\nabla \eta \otimes \nabla \eta) \mathbf{v}_3) \right)^2 \\ &\quad \left. + \left(\frac{\mathbf{v}_1 \cdot \nabla \xi \mathbf{v}_3 + \mathbf{v}_3 \cdot \nabla \xi \mathbf{v}_1}{2} + \frac{\varepsilon}{2} (\mathbf{v}_1 \cdot (\nabla \eta \otimes \nabla \eta) \mathbf{v}_3) \right)^2 \right] d\chi, \end{aligned} \quad (3.11)$$

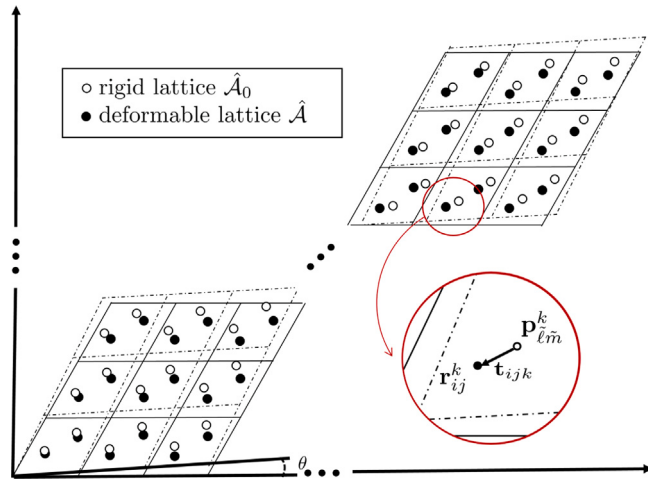


Fig. 3.1. The reference configuration of the system, with \hat{A}_0 and \hat{A} mismatched by an angle θ , in nondimensional coordinates. Only two patches of the lattice structure are shown: near and away from the origin. The region of two atoms in the reference configurations, r_{ij}^k and $p_{\ell\tilde{m}}^k$, is zoomed in to show the corresponding local horizontal mismatched t_{ijk} between them.

and

$$\mathcal{F}_d^\varepsilon[\xi, \eta] =: \gamma_d \varepsilon^3 \int_{D_1} \left[7\eta_{,11}^2 + 16\eta_{,12}^2 - 2\eta_{,11}\eta_{,22} + 7\eta_{,22}^2 \right] d\chi. \quad (3.12)$$

3.2. Van der Waals energy contribution

We derive the continuum versions of (2.10) and (2.12), which we shall see have the form

$$\mathcal{F}_w^\varepsilon[\xi, \eta] = \frac{1}{\varepsilon} \int_{D_1} G(\chi, \xi, \eta) d\chi. \quad (3.13)$$

An important feature of our approach is that, to define the function G , we develop an expression for the local mismatch between the two lattices in their reference configurations. This expression depends on χ and on the relative rotation and lattice parameter mismatch.

The Lennard-Jones potential is considered first. Starting with the inner double sum on the right-hand side of (2.10), we observe that the total interaction energy corresponding to the atom ijk on \hat{A} with all the atoms on the rigid lattice \hat{A}_0 is

$$\sum_{\ell,m=-\infty}^{\infty} \sum_{\tilde{k}=1}^2 g_{\text{LJ}} \left(\frac{\|\mathbf{q}_{ij}^k - \mathbf{p}_{\ell\tilde{m}}^k\|}{\varepsilon} \right). \quad (3.14)$$

Next, we define t_{ijk} , the local horizontal mismatch between the lattices \hat{A}_0 and \hat{A} in the reference configuration as measured at atom ijk on \hat{A} . To determine t_{ijk} , we project the vector \mathbf{r}_{ij}^k onto the plane of \hat{A}_0 . The projection falls inside one of the unit cells of \hat{A}_0 . Let $\tilde{\ell}, \tilde{m}$ be the indices of that unit cell. We define t_{ijk} as the vector from the atom $\mathbf{p}_{\tilde{\ell}\tilde{m}}^k$ on \hat{A}_0 to the endpoint of the projection of \mathbf{r}_{ij}^k onto the plane of \hat{A}_0 . See Fig. 3.1.

We can now write

$$\begin{aligned} \|\mathbf{q}_{ij}^k - \mathbf{p}_{\ell\tilde{m}}^k\| &= \left\| \left(\mathbf{q}_{ij}^k - \mathbf{r}_{ij}^k \right) + \left(\mathbf{r}_{ij}^k - \mathbf{p}_{\tilde{\ell}\tilde{m}}^k \right) + \left(\mathbf{p}_{\tilde{\ell}\tilde{m}}^k - \mathbf{p}_{\ell\tilde{m}}^k \right) \right\| \\ &= \left\| \left(\varepsilon \xi(\chi_{ij}^k), \varepsilon \eta(\chi_{ij}^k) \right) + (\mathbf{t}_{ijk}, \varepsilon) + (\varepsilon \delta_0 ((\tilde{\ell} - \ell + (k - \tilde{k})/3) \mathbf{a}_1^0 + (\tilde{m} - m + (k - \tilde{k})/3) \mathbf{a}_2^0), 0) \right\| \\ &= \left(\left\| \varepsilon \delta_0 ((\tilde{\ell} - \ell + (k - \tilde{k})/3) \mathbf{a}_1^0 + (\tilde{m} - m + (k - \tilde{k})/3) \mathbf{a}_2^0) + \mathbf{t}_{ijk} + \varepsilon \xi(\chi_{ij}^k) \right\|^2 + (\varepsilon + \varepsilon \eta(\chi_{ij}^k))^2 \right)^{1/2}. \end{aligned} \quad (3.15)$$

Recall from (3.4) that $\alpha\varepsilon$, the relative mismatch between the lattice parameters, is $\mathcal{O}(\varepsilon)$. In a similar way, we define

$$\Theta := \frac{\theta}{\varepsilon} = O(1), \quad (3.16)$$

so that $\Theta\varepsilon$, the relative rotation between the lattices, is $\mathcal{O}(\varepsilon)$. Hence, we can linearize \mathbf{t}_{ijk} in ε to write $\mathbf{t}_{ijk} = \mathbf{t}'_{ijk} + \mathbf{t}''_{ijk}$, where \mathbf{t}'_{ijk} is the relative mismatch when $\theta = 0$ and \mathbf{t}''_{ijk} is the relative mismatch when $\alpha = 0$. We next derive expressions for \mathbf{t}'_{ijk} and \mathbf{t}''_{ijk} . Recall that we assume that the left bottom corner of the 0,0 unit cell of \hat{A} lies directly above the left bottom corner of the 0,0 unit cell of \hat{A}_0 .

To write down \mathbf{t}_{ijk}^t , we assume that $\theta = 0$ and hence $\mathbf{a}_i^0 = \mathbf{a}_i$ for $i = 1, 2$. We then have

$$\begin{aligned}\mathbf{t}_{ijk}^t &= \varepsilon\delta((i+k/3)\mathbf{a}_1 + (j+k/3)\mathbf{a}_2) - \varepsilon\delta_0((\tilde{\ell}+k/3)\mathbf{a}_1^0 + (\tilde{m}+k/3)\mathbf{a}_2^0) \\ &= ((i+k/3)(\delta-\delta_0)\varepsilon + i_1\delta_0\varepsilon)\mathbf{a}_1 + ((j+k/3)(\delta-\delta_0)\varepsilon + j_1\delta_0\varepsilon)\mathbf{a}_2 \\ &= \left((i+k/3)\left(\frac{\delta-\delta_0}{\delta\varepsilon}\right)\delta\varepsilon^2 + i_1\delta_0\varepsilon\right)\mathbf{a}_1 + \left((j+k/3)\left(\frac{\delta-\delta_0}{\delta\varepsilon}\right)\delta\varepsilon^2 + j_1\delta_0\varepsilon\right)\mathbf{a}_2 \\ &= \alpha\varepsilon(\delta\varepsilon(i+k/3))\mathbf{a}_1 + \alpha\varepsilon(\delta\varepsilon(j+k/3))\mathbf{a}_2 + \delta_0\varepsilon i_1\mathbf{a}_1 + \delta_0\varepsilon j_1\mathbf{a}_2 = \alpha\varepsilon\chi_{ij}^k + \delta_0\varepsilon(i_1\mathbf{a}_1 + j_1\mathbf{a}_2),\end{aligned}\quad (3.17)$$

where $i_1 = i - \tilde{\ell}$ and $j_1 = j - \tilde{m}$, and where the final equal sign uses (3.5). Note that we could instead write

$$\mathbf{t}_{ijk}^t = \alpha\varepsilon\chi_{ij}^k + \delta_0\varepsilon(i_1\mathbf{a}_1^0 + j_1\mathbf{a}_2^0). \quad (3.18)$$

To write down \mathbf{t}_{ijk}^r , we assume $\delta_0 = \delta$, and in this case, we have

$$\begin{aligned}\mathbf{t}_{ijk}^r &= \varepsilon\delta_0((i+k/3)\mathbf{a}_1 + (j+k/3)\mathbf{a}_2) - \varepsilon\delta_0((\tilde{\ell}+k/3)\mathbf{a}_1^0 + (\tilde{m}+k/3)\mathbf{a}_2^0) \\ &= \varepsilon\delta_0((i+k/3)(\mathbf{a}_1 - \mathbf{a}_1^0) + (j+k/3)(\mathbf{a}_2 - \mathbf{a}_2^0)) + \varepsilon\delta_0(i_2\mathbf{a}_1^0 + j_2\mathbf{a}_2^0),\end{aligned}\quad (3.19)$$

where $i_2 = i - \tilde{\ell}$ and $j_2 = j - \tilde{m}$. Recalling that the lattice $\hat{\mathcal{A}}_0$ is rotated with respect to $\hat{\mathcal{A}}$ by the angle $\theta = \varepsilon\Theta$, we see that

$$\mathbf{a}_i - \mathbf{a}_i^0 = \mathbf{a}_i - R(\theta)\mathbf{a}_i = \begin{pmatrix} 1 - \cos\varepsilon\Theta & \sin\varepsilon\Theta \\ -\sin\varepsilon\Theta & 1 - \cos\varepsilon\Theta \end{pmatrix}\mathbf{a}_i \approx \varepsilon\Theta\begin{pmatrix} 0 & 1 \\ -1 & 0 \end{pmatrix}\mathbf{a}_i \quad \text{for } i = 1, 2.$$

Inserting these expressions into (3.19) yields

$$\mathbf{t}_{ijk}^r \approx \varepsilon\Theta(\chi_{ij}^k)^\perp + \varepsilon\delta_0(i_2\mathbf{a}_1^0 + j_2\mathbf{a}_2^0), \quad (3.20)$$

where $(\chi_{ij}^k)^\perp = \begin{pmatrix} 0 & 1 \\ -1 & 0 \end{pmatrix}\chi_{ij}^k$.

Combining (3.18) and (3.20) gives

$$\mathbf{t}_{ijk} = \mathbf{t}_{ijk}^t + \mathbf{t}_{ijk}^r \approx \alpha\varepsilon\chi_{ij}^k + \varepsilon\Theta(\chi_{ij}^k)^\perp + \varepsilon\delta_0(i_1\mathbf{a}_1^0 + j_1\mathbf{a}_2^0 + i_2\mathbf{a}_1^0 + j_2\mathbf{a}_2^0). \quad (3.21)$$

Now we substitute (3.21) into (3.15). Also, we use that $i_1 = i_2 = i - \tilde{\ell}$, $j_1 = j_2 = j - \tilde{m}$ and that the basis of $\hat{\mathcal{A}}_0$ is a small perturbation of the basis of $\hat{\mathcal{A}}$, which follows from the smallness of θ . Lastly, we use that δ_0 and δ are close. From (3.15), we thereby obtain

$$\begin{aligned}\|\mathbf{q}_{ij}^k - \mathbf{p}_{\ell m}^{\tilde{k}}\| &\approx \varepsilon\left(\left\|\delta_0((\tilde{\ell}-\ell+(k-\tilde{k})/3)\mathbf{a}_1^0 + (\tilde{m}-m+(k-\tilde{k})/3)\mathbf{a}_2^0 + 2i_1\mathbf{a}_1^0 + 2j_1\mathbf{a}_2^0)\right.\right. \\ &\quad \left.\left.+ \alpha\chi_{ij}^k + \Theta(\chi_{ij}^k)^\perp + \xi(\chi_{ij}^k)\right\|^2 + (1+\eta(\chi_{ij}^k))^2\right)^{\frac{1}{2}} \\ &\approx \varepsilon\left(\delta_0((2i-\ell-\tilde{\ell}+(k-\tilde{k})/3)\mathbf{a}_1^0 + (2j-m-\tilde{m}+(k-\tilde{k})/3)\mathbf{a}_2^0)\right. \\ &\quad \left.\left.+ \alpha\chi_{ij}^k + \Theta(\chi_{ij}^k)^\perp + \xi(\chi_{ij}^k)\right\|^2 + (1+\eta(\chi_{ij}^k))^2\right)^{\frac{1}{2}} \\ &\approx \varepsilon\left(\left\|\delta((2i-\ell-\tilde{\ell}+(k-\tilde{k})/3)\mathbf{a}_1 + (2j-m-\tilde{m}+(k-\tilde{k})/3)\mathbf{a}_2)\right.\right. \\ &\quad \left.\left.+ \alpha\chi_{ij}^k + \Theta(\chi_{ij}^k)^\perp + \xi(\chi_{ij}^k)\right\|^2 + (1+\eta(\chi_{ij}^k))^2\right)^{\frac{1}{2}} \\ &= \varepsilon\left(\left\|\delta((\ell+(k-\tilde{k})/3)\mathbf{a}_1 + (m+(k-\tilde{k})/3)\mathbf{a}_2)\right.\right. \\ &\quad \left.\left.+ \alpha\chi_{ij}^k + \Theta(\chi_{ij}^k)^\perp + \xi(\chi_{ij}^k)\right\|^2 + (1+\eta(\chi_{ij}^k))^2\right)^{\frac{1}{2}},\end{aligned}\quad (3.22)$$

where in the last line we changed the indices $\ell \rightarrow 2i - \ell - \tilde{\ell}$ and $m \rightarrow 2j - m - \tilde{m}$. Therefore, we can write

$$g_{\text{LJ}}\left(\frac{\|\mathbf{q}_{ij}^k - \mathbf{p}_{\ell m}^{\tilde{k}}\|}{\varepsilon}\right) = g_{\text{LJ}}\left(\sqrt{\rho\left(\alpha\chi_{ij}^k + \Theta(\chi_{ij}^k)^\perp + \xi(\chi_{ij}^k)\right)^2 + (1+\eta(\chi_{ij}^k))^2}\right), \quad (3.23)$$

where

$$\rho(\mathbf{p}) = \|\delta(\ell+(k-\tilde{k})/3)\mathbf{a}_1 + \delta(m+(k-\tilde{k})/3)\mathbf{a}_2 + \mathbf{p}\|$$

for every $\mathbf{p} \in \mathbb{R}^2$.

To complete the definition of G for the Lennard-Jones potential, we now set

$$G(\chi, \xi, \eta) := G_{\text{LJ}}(\alpha\chi + \Theta\chi^\perp + \xi, \eta), \quad (3.24)$$

where

$$\mathcal{G}_{\text{LJ}}(\mathbf{p}, t) := \sum_{k=1}^2 \sum_{\ell, m=-\infty}^{\infty} \sum_{\bar{k}=1}^2 g_{\text{LJ}} \left(\sqrt{\rho(\mathbf{p})^2 + (1+t)^2} \right) \quad (3.25)$$

for $t > -1$.

For the Kolmogorov–Crespi potential, we note that $\rho \left(\alpha \chi_{ij}^k + \Theta(\chi_{ij}^k)^\perp + \xi \left(\chi_{ij}^k \right) \right)$ is the length of the projection of $\mathbf{q}_{ij}^k - \mathbf{p}_{\ell m}^{\bar{k}}$ onto the xy -plane, which is the plane containing the fixed lattice $\hat{\mathcal{A}}_0$. In this case, we set

$$G(\chi, \xi, \eta) := \mathcal{G}_{\text{KC}} \left(\alpha \chi + \Theta \chi^\perp + \xi, \eta \right),$$

where

$$\mathcal{G}_{\text{KC}}(\mathbf{p}, t) := \sum_{k=1}^2 \sum_{\ell, m=-\infty}^{\infty} \sum_{\bar{k}=1}^2 g_{\text{KC}} \left(\sqrt{\rho(\mathbf{p})^2 + (1+t)^2}, \frac{\epsilon \rho(\mathbf{p})}{\delta/L} \right). \quad (3.26)$$

Finally, the nondimensional version of either (2.10) or (2.12) takes the form

$$\mathcal{E}_w = \epsilon \sum_{i,j=1}^N \sum_{k=1}^2 \sum_{\ell, m=-\infty}^{\infty} \sum_{\bar{k}=1}^2 g \approx \frac{1}{\epsilon} \sum_{i,j=1}^N G(\chi, \xi, \eta) \epsilon^2 \approx \frac{1}{\epsilon} \int_{D_1} G(\chi, \xi, \eta) d\chi =: \mathcal{F}_w^\epsilon[\xi, \eta], \quad (3.27)$$

where g is either g_{LJ} or g_{KC} with the appropriate arguments and G is defined using either \mathcal{G}_{LJ} or \mathcal{G}_{KC} . This establishes (3.13).

3.3. Continuum energy

Combining (3.10)–(3.12) and (3.27) yields a continuum energy functional that can be written as

$$\begin{aligned} \mathcal{F}^\epsilon[\xi, \eta] := & \frac{\epsilon}{2} \int_{D_1} f \left(D(V \nabla \xi V^T) + \frac{\epsilon}{2} V (\nabla \eta \otimes \nabla \eta) V^T \right) d\chi \\ & + \gamma_d \epsilon^3 \int_{D_1} \left[7\eta_{,11}^2 + 16\eta_{,12}^2 - 2\eta_{,11}\eta_{,22} + 7\eta_{,22}^2 \right] d\chi + \frac{1}{\epsilon} \int_{D_1} G(\chi, \xi, \eta) d\chi. \end{aligned} \quad (3.28)$$

Here $D(A) = (A + A^T)/2$ is the symmetric part of A for any $A \in M^{3 \times 3}$, V is the 3×2 matrix whose i th row is \mathbf{v}_i and

$$f(M) = \gamma_s (m_{11}^2 + m_{22}^2 + m_{33}^2) + \gamma_t (m_{12}^2 + m_{21}^2 + m_{13}^2 + m_{31}^2 + m_{23}^2 + m_{32}^2)$$

for any $M = (m_{ij}) \in M_{\text{sym}}^{3 \times 3}$.

Note that the elastic contribution to the energy (3.28) is like that of the Föppl–von Kármán theory. The corresponding variational problem is of Ginzburg–Landau type, where the minimizers are determined via a competition between the elastic energy and the potential energy, which has multiple wells associated with the low-energy commensurate regions. The system is forced to reside in these wells, with the sharp transition between the wells being smoothed out due to the penalty imposed by the elastic energy. Consequently, we expect the minimizers of (3.28) to develop walls of characteristic width ϵ .

Now let $B(\nabla \xi, \nabla \eta) = D(V \nabla \xi V^T) + \frac{\epsilon}{2} V \nabla \eta \otimes \nabla \eta V^T$ and

$$\hat{M} = \begin{pmatrix} \gamma_s B_{11} & \gamma_t B_{12} & \gamma_t B_{13} \\ \gamma_t B_{21} & \gamma_s B_{22} & \gamma_t B_{23} \\ \gamma_t B_{31} & \gamma_t B_{32} & \gamma_s B_{33} \end{pmatrix},$$

where B_{ij} are the entries in the matrix $B(\nabla \xi, \nabla \eta)$. Let $\mathbf{b}_1(\nabla \xi, \nabla \eta)$ and $\mathbf{b}_2(\nabla \xi, \nabla \eta)$ be the first two columns of $V^T \hat{M} V$. It is shown in Supplementary Material that the Euler–Lagrange equations for the functional \mathcal{F}^ϵ are

$$\begin{cases} -\epsilon \operatorname{div} [\mathbf{b}_1(\nabla \xi, \nabla \eta)] + \frac{1}{\epsilon} \frac{\partial G}{\partial \xi_1}(\chi, \xi, \eta) = 0, \\ -\epsilon \operatorname{div} [\mathbf{b}_2(\nabla \xi, \nabla \eta)] + \frac{1}{\epsilon} \frac{\partial G}{\partial \xi_2}(\chi, \xi, \eta) = 0, \\ 14\epsilon^3 \gamma_d \Delta^2 \eta - \epsilon^2 \operatorname{div} (\mathbf{b}_1(\nabla \xi, \nabla \eta) \cdot \nabla \eta, \mathbf{b}_2(\nabla \xi, \nabla \eta) \cdot \nabla \eta) + \frac{1}{\epsilon} \frac{\partial G}{\partial \eta}(\chi, \xi, \eta) = 0. \end{cases} \quad (3.29)$$

Here the first two equations describe the force balance in the plane of the deformable lattice, while the last equation is the vertical force balance.

4. Numerical results

To validate our discrete-to-continuum procedure, in this section we compare the predictions of the discrete and the continuum models. We consider results for both the Lennard-Jones 12–6 potential (2.11) and the Kolmogorov–Crespi potential (2.13). To solve the atomistic model numerically, we use LAMMPS (Plimpton, 1995) to minimize the discrete energy (2.5). We use COMSOL (com, 0000) to numerically solve the system of partial differential Eqs. (3.29) derived from the continuum model (3.28). For the continuum

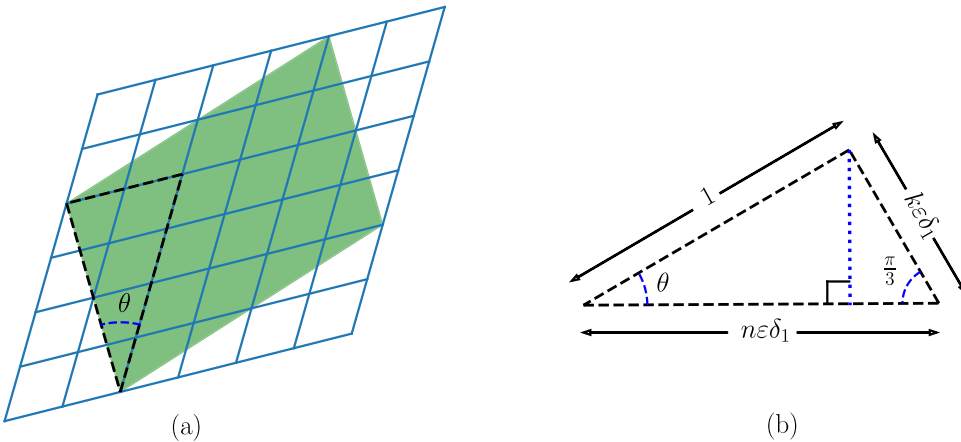


Fig. 4.1. (a) A rotation of the reference configuration \mathcal{A}^0 (shaded) such that each corner sits above a corner of a unit cell in $\hat{\mathcal{A}}_0$. (b) Geometry of the dashed triangle in (a). In the case depicted, $k = 2$ and $n = 4$.

simulations, we use dissipation-dominated (gradient flow) dynamics to drive the energy of the system toward a possibly local minimum. The same task was accomplished for the atomistic model by performing molecular dynamics simulations at a sufficiently low temperature.

For the simulations, we choose numerical values for the parameters that appear in the discrete model. The parameters in the continuum model are then determined by the rescaling. The values we use for k_s , k_t , and k_d , which describe the bonded interactions in the discrete model, are not chosen to be appropriate for graphene. In part this is because, to accurately describe graphene, we should be using more sophisticated potentials. We use simple interatomic potentials here to facilitate the upscaling procedure, which is the focus of this paper. A second reason is that our main goal with the simulations is to illustrate a qualitative match in the moiré patterns predicted by the discrete and the continuum models. For the parameters in Lennard-Jones model, we also do not use parameters realistic for graphene. On the other hand, for the additional parameters that appear in the Kolmogorov-Crespi potential we use a standard set of values describing graphene, as these were readily available in LAMMPS. Extending our upscaling procedure to more realistic potentials that accurately describe graphene is something we intend to explore in future work. This is discussed briefly in the concluding section.

4.1. Periodic boundary conditions

In this subsection we describe how the boundary conditions are implemented in the simulations below. Recall that we assume that $\hat{\mathcal{A}}$ is infinite in extent and deforms periodically. Periodicity requires that the surface \mathcal{A}^0 satisfies the following constraint. If we pick two points identified on the edges of \mathcal{A}^0 and project the position vectors for these points onto $\hat{\mathcal{A}}_0$, then $\hat{\mathcal{A}}_0$ is invariant when translated by the vector between the two projected points. See Fig. 4.1(a). This in turn places constraints on the combinations of rotation and lattice mismatch that can be used to define the reference configuration.

As suggested by Fig. 4.1(a), a sufficient condition for periodicity is that each corner of the reference configuration \mathcal{A}^0 sits above a corner of a unit cell in $\hat{\mathcal{A}}_0$. From the triangle in Fig. 4.1(b), we derive the relations

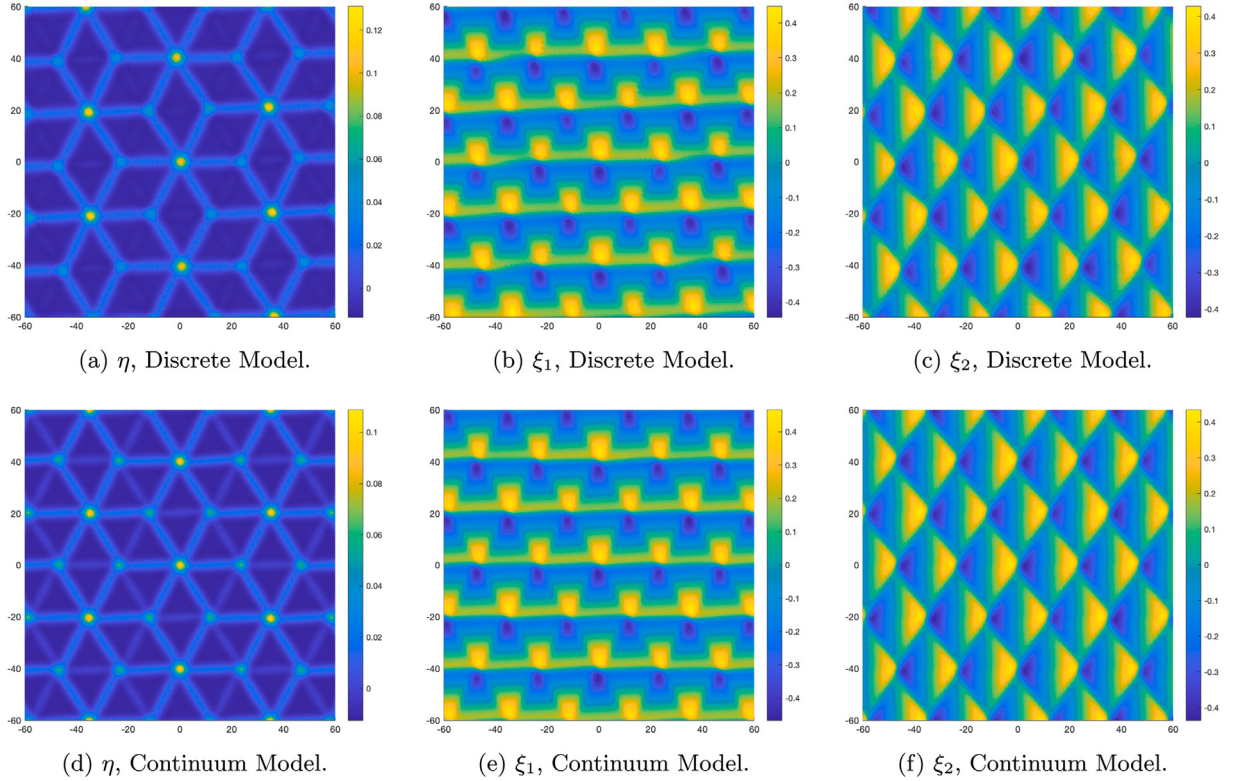
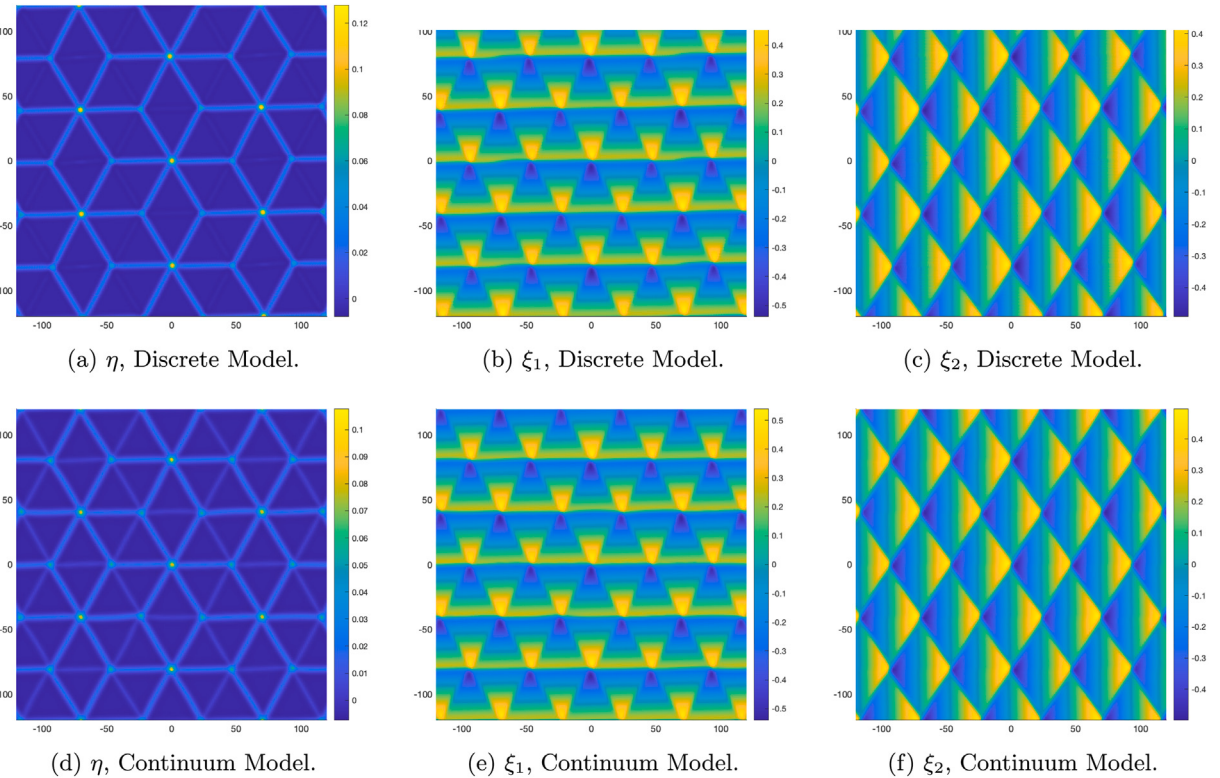
$$\cos \theta = n\epsilon\delta_0 - \frac{1}{2}k\epsilon\delta_0, \quad \sin \theta = \frac{\sqrt{3}}{2}k\epsilon\delta_0, \quad \text{and} \quad \tan \theta = \frac{\frac{\sqrt{3}}{2}k}{n - \frac{k}{2}} \quad (4.1)$$

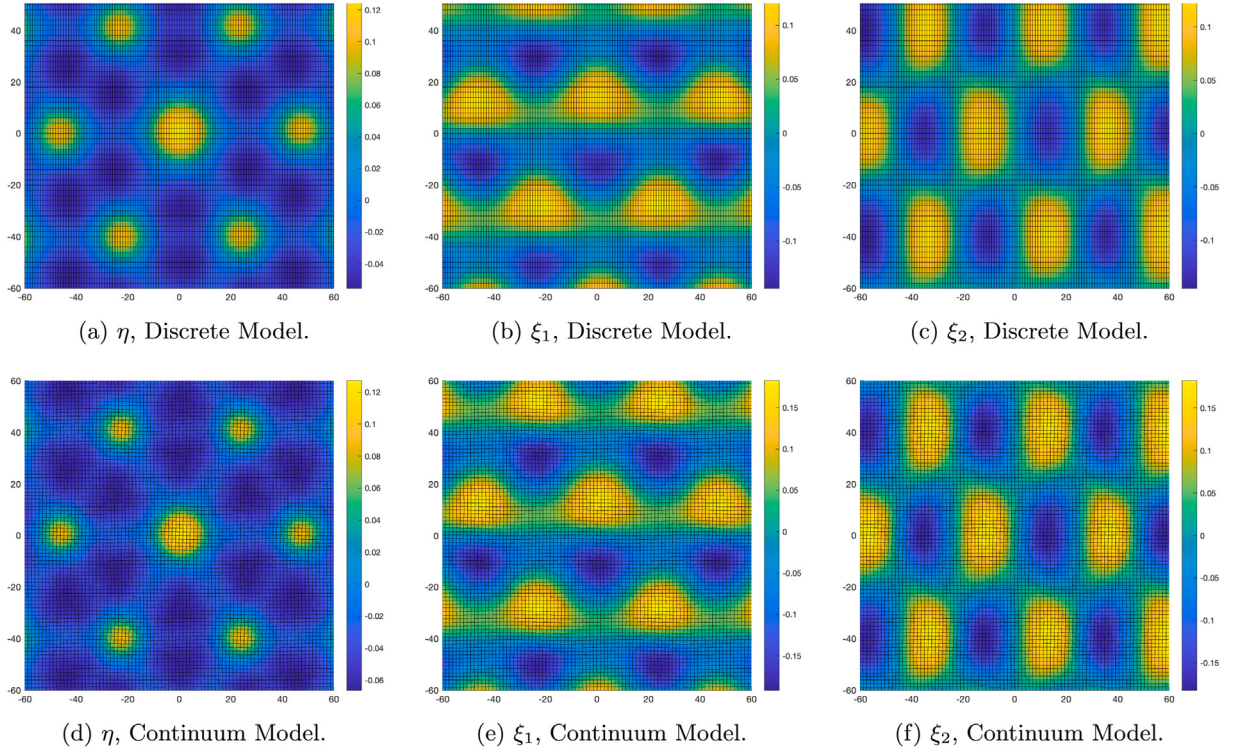
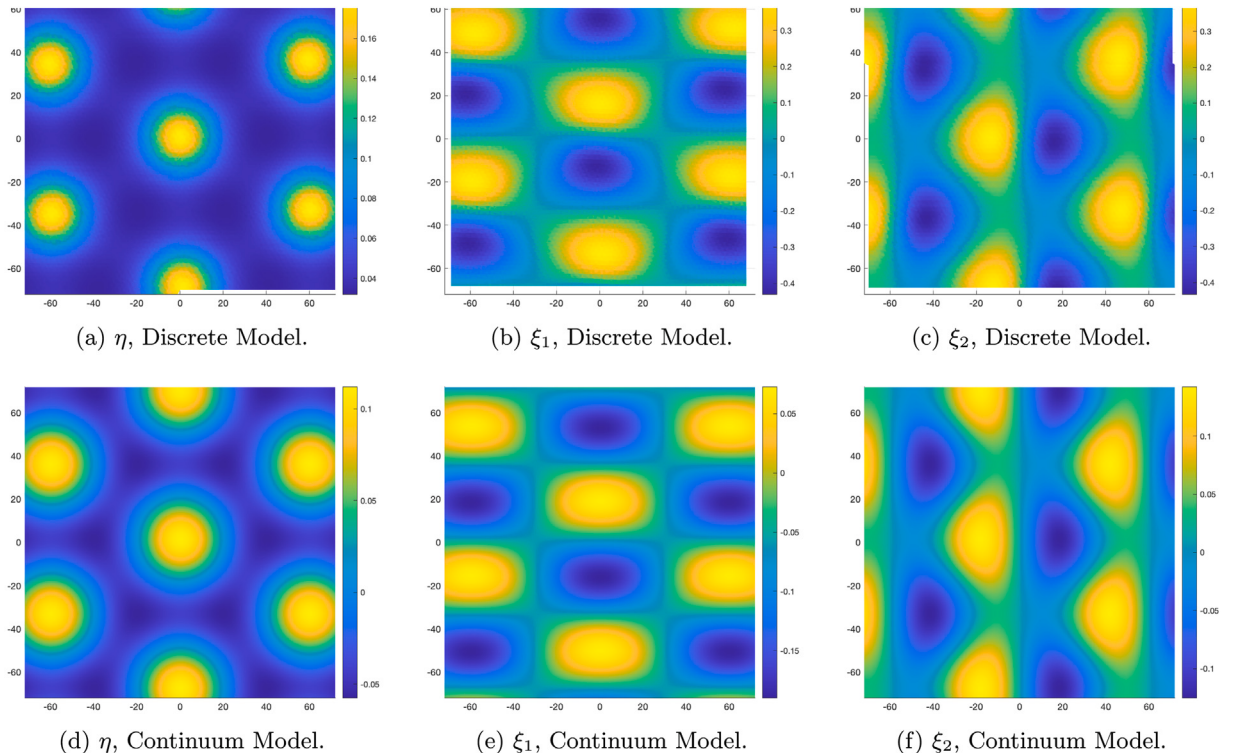
among θ , $\epsilon\delta_0$, n , and k .

We use (4.1) to generate parameter values ensuring that periodicity is satisfied. Recall that we denote the number of unit cells in each side of the deformable lattice $\hat{\mathcal{A}}$ in D_1 by N , so that $\epsilon\delta N = 1$. We pick N and δ and set $\epsilon = (\delta N)^{-1}$. Given ϵ , we pick $k, n \in \mathbb{N}$ and set

$$\theta := \arctan\left(\frac{\frac{\sqrt{3}}{2}k}{n - \frac{k}{2}}\right) \quad \text{and} \quad \delta_0 := \frac{2}{\sqrt{3}k\epsilon} \sin \theta = \frac{1}{\epsilon\sqrt{\left(n - \frac{k}{2}\right)^2 + \frac{3}{4}k^2}}. \quad (4.2)$$

Note that the first condition in (4.1) is also satisfied. Hence the reference configuration will satisfy the ‘corner-to-corner’ periodicity condition.

Fig. 4.2. Simulation Results for Lennard-Jones Potential with $\epsilon = 0.0094$ and $\omega = 0.5$.Fig. 4.3. Simulation Results for Lennard-Jones Potential with $\epsilon = 0.0047$ and $\omega = 0.5$.

Fig. 4.4. Simulation Results for Lennard-Jones Potential with $\varepsilon = 0.0047$ and $\omega = 0.0083$.Fig. 4.5. Simulation Results for Kolmogorov-Crespi Potential with $\varepsilon = 0.024$.

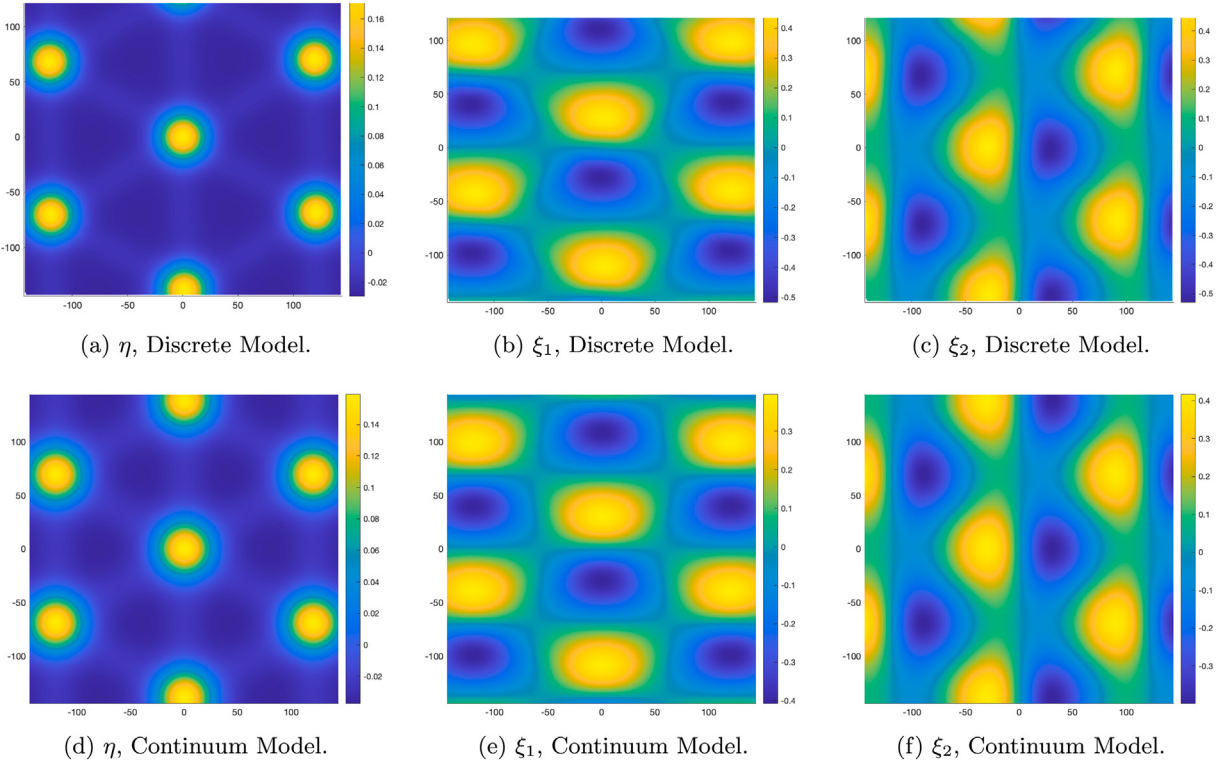


Fig. 4.6. Simulation Results for Kolmogorov–Crespi Potential with $\varepsilon = 0.012$.

Next we use (4.2) to derive useful expressions for the parameters α and Θ appearing in (3.24). We define m by $n = N - m$. From (3.16) we have

$$\Theta = \frac{\theta}{\varepsilon} = \frac{1}{\varepsilon} \arctan \left(\frac{\frac{\sqrt{3}}{2} k \varepsilon \delta}{n \varepsilon \delta - \frac{k}{2} \varepsilon \delta} \right) = \frac{1}{\varepsilon} \arctan \left(\frac{\frac{\sqrt{3}}{2} k \delta \varepsilon}{1 - \left(m + \frac{k}{2} \right) \delta \varepsilon} \right) \approx \frac{\sqrt{3}}{2} k \delta, \quad (4.3)$$

using that $\varepsilon \delta N = 1$. Further,

$$\alpha = \frac{\delta_0 - \delta}{\varepsilon \delta} = \frac{1}{\varepsilon^2 \delta \sqrt{\left(N - m - \frac{k}{2} \right)^2 + \frac{3}{4} k^2}} - 1 = \frac{1}{\varepsilon \sqrt{\left(1 - \left(m + \frac{k}{2} \right) \varepsilon \delta \right)^2 + \frac{3}{4} (\varepsilon \delta k)^2}} - 1 \approx \left(m + \frac{k}{2} \right) \delta. \quad (4.4)$$

4.2. Results for the Lennard-Jones potential

For the Lennard-Jones potential, we start by comparing results for two different values of ε . Fig. 4.2 shows results for $\varepsilon = 0.0094$ and Fig. 4.3 shows results for $\varepsilon = 0.0047$. Each set of plots shows the out-of-plane displacement η and the two in-plane displacements ξ_1 and ξ_2 for both the discrete and continuum models. The parameter values used in these simulations are given in Tables 4.1(a), (b).

In the plots shown in Fig. 4.3, the lateral extent of the system is twice the lateral extent of the plots in Fig. 4.2. This difference reflects how changes in ε are implemented in the discrete simulations. The continuum simulations are based on the partial differential Eqs. (3.29), in which ε appears explicitly. Hence we directly set the value of ε . However, ε does not appear explicitly in the discrete energy. Instead, recalling that $\varepsilon = \sigma/L$ we run simulations corresponding to different values of ε by changing the lateral size L of the system, i.e., by making the fixed and the deformable lattices smaller or larger.

The main observation from Figs. 4.2 and 4.3 is that for both values of ε , we see good agreement between the discrete and the continuum models. We note that, for the out-of-plane displacement η , our simulations predict spatial patterns that have been observed for twisted graphene bilayers in many studies (van Wijk et al., 2015, 2014; Nam and Koshino, 2017; Jain et al., 2016; Enaldiev et al., 2020). The plots of η in Figs. 4.2(a), 4.2(d), 4.3(a), and 4.3(d) exhibit hot spots, which are regions of relatively large out-of-plane displacement localized about a point. Neighboring hot spots are connected by straight ridges or wrinkles, which are regions of relatively large out-of-plane displacement localized about the lines joining the hot spots. These wrinkles form domain walls between relatively large triangular commensurate regions.

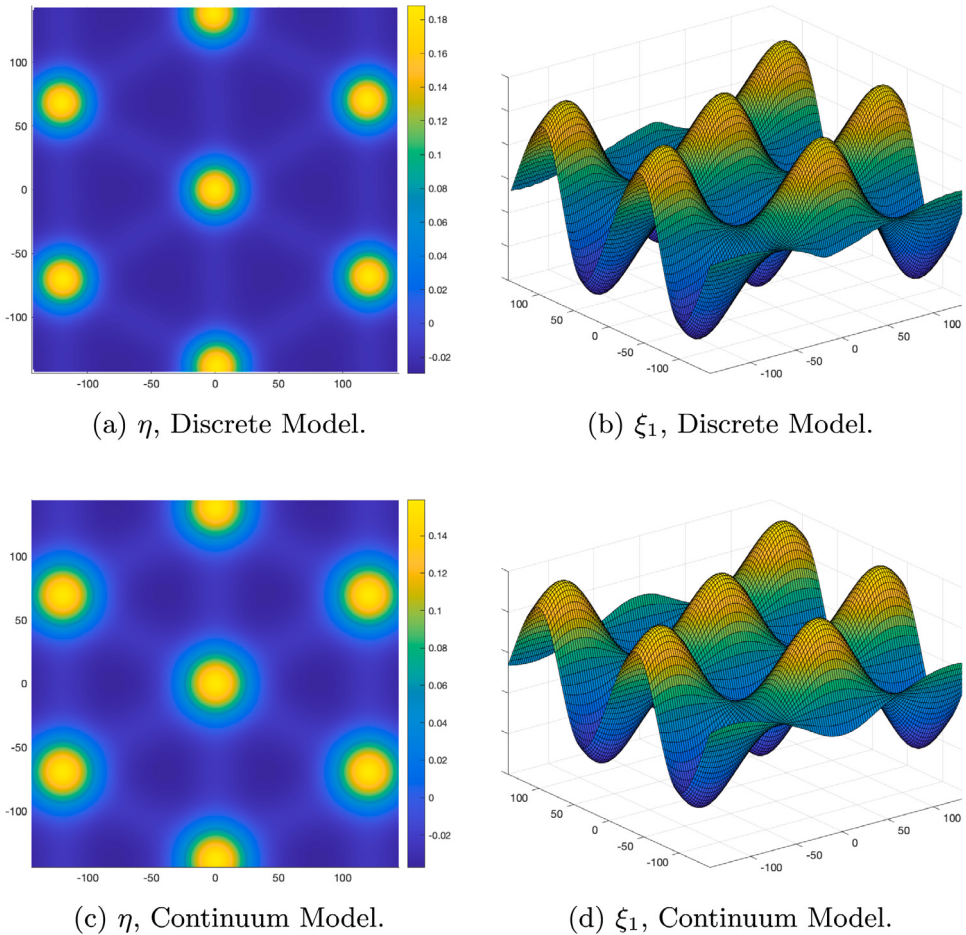


Fig. 4.7. Simulation Results for the Kolmogorov–Crespi Potential, Large Elastic Constants.

In this same set of plots, we see that the hot spots occur at two different possible heights. In this case, we refer to the wrinkles emanating from the higher hot spots as *primary wrinkles* and the other wrinkles, which connect two lower hot spots, as *secondary wrinkles*. We note that the secondary wrinkles are less discernible in the plots from the discrete simulations compared to the plots from the continuum simulations. We can see this when comparing Figs. 4.2(a) and 4.2(d) and when comparing Figs. 4.3(a) and 4.3(d). In Fig. 4.3(a), it is difficult to discern any secondary wrinkles. Another observation is that as ϵ decreases, the hot spots and the connecting wrinkles become more spatially concentrated, as expected by the form of the energy for the continuum model.

Next, we consider the effect of changing the value of the parameter ω , which appears in the Lennard-Jones potential and measures the strength of the interaction, or the well-depth. See (2.10). Recall that we rescale the discrete energy by ω when we derived the continuum model. Decreasing ω increases the value of the dimensionless elastic constants γ_s , γ_t , and γ_d . We consider results for two values of ω . In Fig. 4.3, we see results for $\omega = 0.5$.

We now compare these plots to the results depicted in Fig. 4.4, for which the parameter values are the same as those used for Fig. 4.3 except that $\omega = 0.0083$ and that consequently the values of γ_s , γ_t , and γ_d are different. See Tables 4.1(a), (b). Note that the difference in lateral extent seen in these two sets of plots is not because ϵ is different. Rather, in Fig. 4.4, we show only a subset of the full domain in order to better exhibit the details of each plot. We see that for a smaller value of ω , the hot spots and the wrinkles become more spatially diffuse and the triangular commensurate regions occupy a relatively smaller part of the lattice. For smaller ω , there is better agreement between the results predicted by the discrete and the continuum models. In particular, we see good agreement between the heights of the secondary wrinkles when comparing Figs. 4.4(a) to 4.4(d). Decreasing the value of ω improves the match because it increases the ratio of the elastic constants to the interaction constant. See Español et al. (2017) for further discussion of this issue.

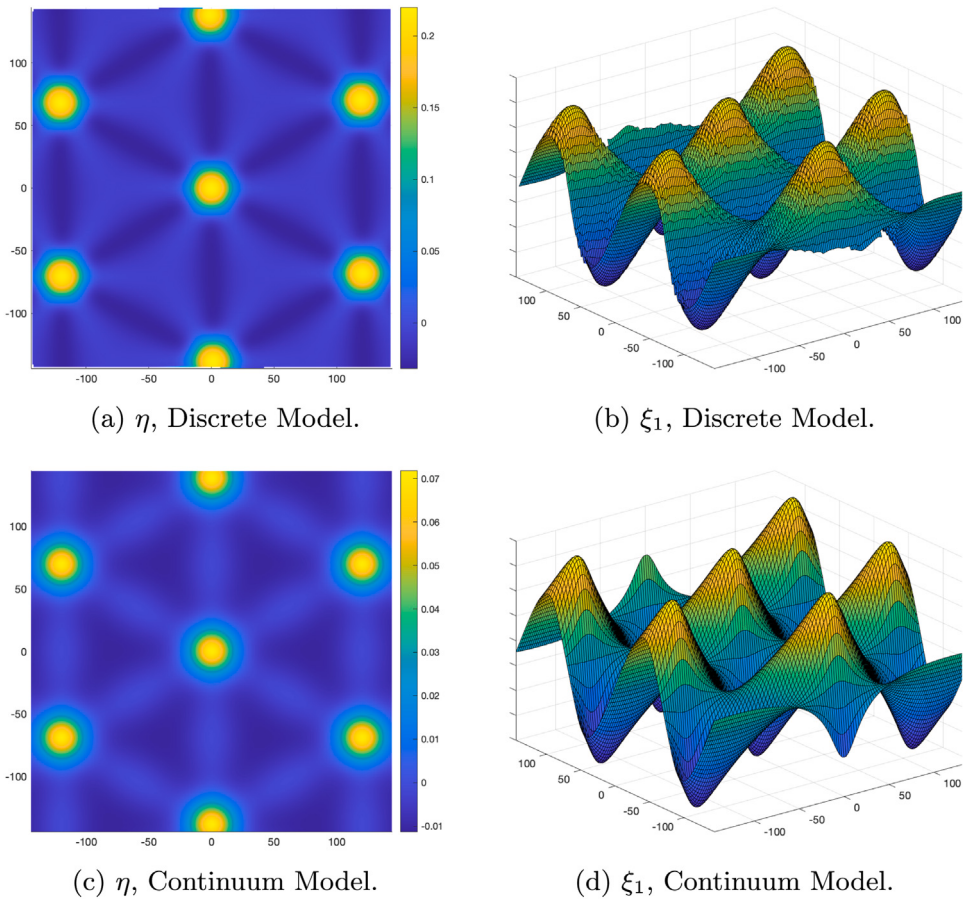


Fig. 4.8. Simulation Results for the Kolmogorov–Crespi Potential, Small Elastic Constants.

Table 4.1

Parameter values for simulations using LJ potential.

(a) Parameters for the discrete model. All lengths are in Å. θ is in degrees. k_s , k_t , k_d , and ω are in eV.

	h_0 , h	L	θ	k_s	k_t	k_d	σ	ω
Figs. 4.2	$3^{1/2}2^{1/6}$	120	-3.22	25.2	1.5375	4.1	$2^{1/6}$	0.5
Figs. 4.3	$3^{1/2}2^{1/6}$	240	-1.6	25.2	1.5375	4.1	$2^{1/6}$	0.5
Figs. 4.4	$3^{1/2}2^{1/6}$	240	-1.6	25.2	1.5375	4.1	$2^{1/6}$	0.008

(b) Dimensionless parameters for the continuum model. Θ is in radians.

	ϵ	δ_0 , δ	k	m	α	Θ	γ_s	γ_t	γ_d
Figs. 4.2	0.0094	$3^{1/2}$	4	-2	0	-6	174.58	113.62	3.55
Figs. 4.3	0.0047	$3^{1/2}$	4	-2	0	-6	174.58	113.62	3.55
Figs. 4.4	0.0047	$3^{1/2}$	4	-2	0	-6	10474.79	6817.35	213.04

4.3. Results for the Kolmogorov–Crespi potential

In this subsection, we compare the predictions of the discrete and continuum models for the Kolmogorov–Crespi potential. For the discrete simulations, we generate results using the potential in (2.13), which we refer to as the Kolmogorov–Crespi-z potential.

To demonstrate that the match between the discrete and the continuum improves as ϵ gets smaller, we consider results for two different values of ϵ . Fig. 4.5 shows results for $\epsilon = 0.024$. Fig. 4.6 shows results for $\epsilon = 0.012$. The other parameter values used in these simulations are listed in

Tables 4.2(a), (b), and (c). As in the previous subsection, the main point is the good match we see between the predictions of the discrete and continuum models. Also, as we saw above, here we see by comparing Figs. 4.5(a) and 4.6(a) and by comparing Figs. 4.5(d) and 4.6(d) that reducing ϵ spatially concentrates the hotspots and the wrinkles.

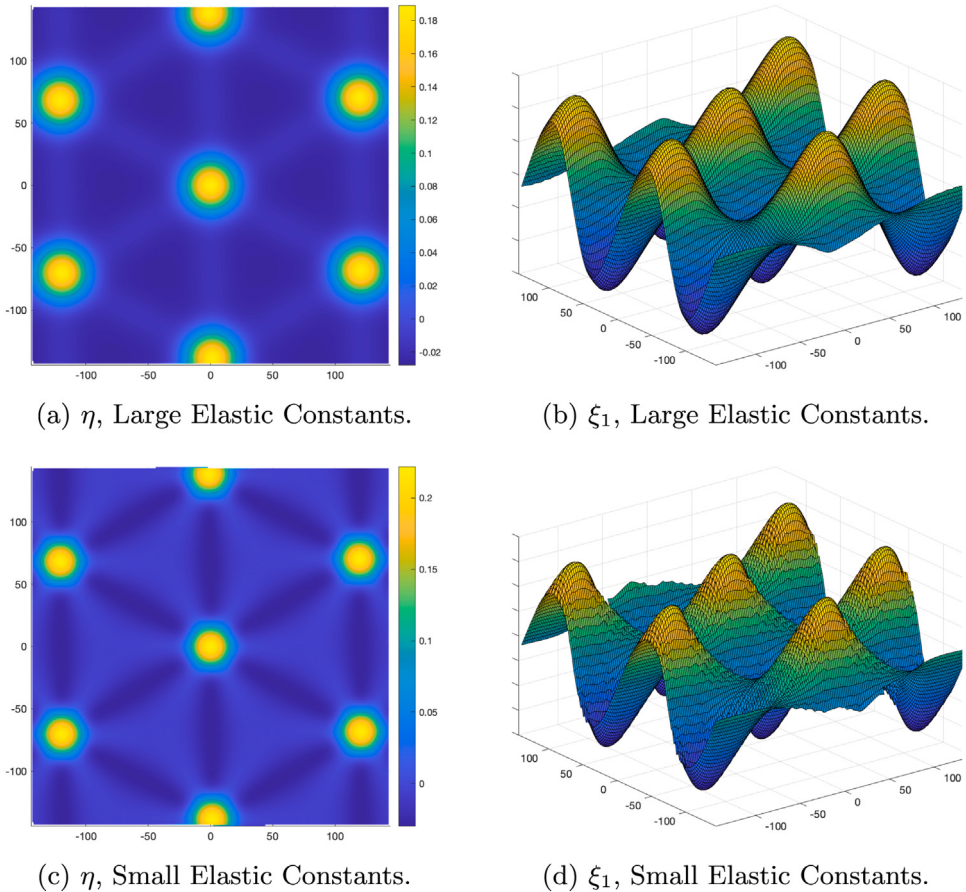


Fig. 4.9. Simulation Results for the Discrete Model Using the Full Kolmogorov–Crespi Potential.

Table 4.2
Parameter values for simulations using KC potential.

(a) Parameters for the discrete model. All lengths are in Å. θ is in degrees. k_s , k_t , k_d , and ω are in eV.									
h_0 , h	L	θ	k_s	k_t	k_d	σ	ω	$\tilde{\delta}$	
Fig. 4.5	2.46	140	-1.74	3.23	0.75	12.0	3.34	0.01	0.58
Fig. 4.6	2.46	280	-0.87	3.23	0.75	12.0	3.34	0.01	0.58

(b) Dimensionless parameters for the continuum model. Θ is in radians.									
ϵ	δ_0 , δ	k	m	α	Θ	γ_s	γ_t	γ_d	
Fig. 4.5	0.024	0.74	2	-1	0	-1.28	123.66	306.64	10.39
Fig. 4.6	0.012	0.74	2	-1	0	-1.28	123.66	306.64	10.39

(c) Dimensionless parameters for the KC potential.				
$\tilde{\lambda}$	\tilde{C}	\tilde{C}_0	\tilde{C}_2	\tilde{C}_4
12.12	0.30	1.53	1.20	0.48

4.4. Results for two versions of the Kolmogorov–Crespi potential

Here we compare results based on the full Kolmogorov–Crespi potential (Kolmogorov and Crespi, 2005) to results based on the Kolmogorov–Crespi-z potential (2.13). We compare the predictions of the discrete model using both these potentials to the predictions of the continuum model, which is derived using the Kolmogorov–Crespi-z potential. Note that we do not have a version of the continuum model derived from the full Kolmogorov–Crespi potential. The goal of these comparisons is to explain why in some cases we fail to see a good match between the predictions of the discrete and the continuum models.

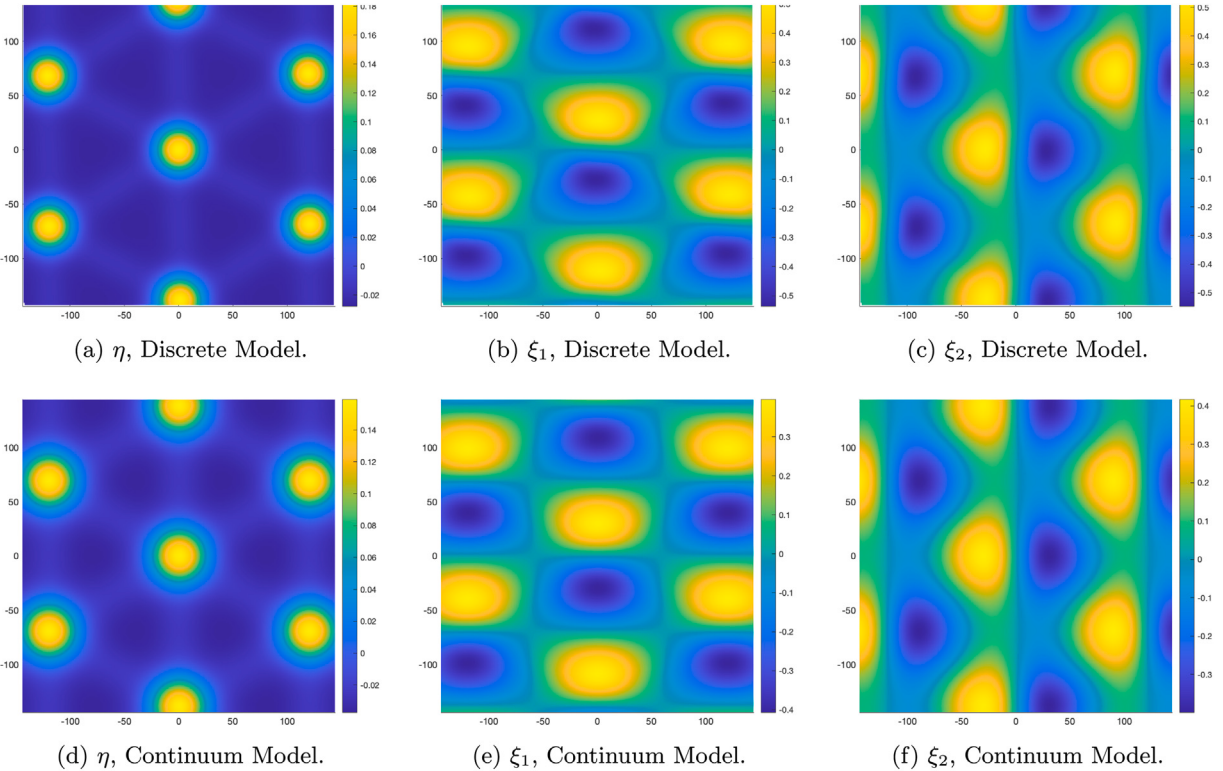


Fig. 4.10. Simulation Results for the Kolmogorov–Crespi Potential, Large Elastic Constants.

We present a set of results that indicates how the size of the elastic constants affects the smoothness of the deformed configurations. We consider two cases, one case in which the elastic constants are relatively small and one case in which the elastic constants are relatively large. The parameter values used in the simulations are listed in Tables 4.3 (a), (b) and 4.2(c).

In Fig. 4.7, we show results based on the Kolmogorov–Crespi-z potential for the case when the elastic constants are relatively large. The key plot here is Fig. 4.7(b), which shows that the discrete model predicts smooth deformations. Comparing the LAMMPS results to the COMSOL results in this set of figures, we see that we get a good match between the predictions of the discrete and continuum models. Note in particular that in both Figs. 4.7(a) and 4.7(c), the secondary wrinkles deflect away from the fixed lattice, i.e., the wrinkles are higher than the surrounding commensurate regions.

In Figs. 4.8, we show results based on the Kolmogorov–Crespi-z potential for the case when the elastic constants are relatively small. In this case, we get a poor match between the predictions of the discrete and continuum models. In particular, Fig. 4.8(a) indicates that the primary and secondary wrinkles deflect toward the fixed lattice for the discrete model, while Fig. 4.8(c) indicates that the primary and secondary wrinkles deflect away from the fixed lattice for the continuum model. A key observation here is that when the elastic constants are small, the deformed configuration predicted by the discrete simulation exhibits small-scale spatial oscillation, as can be seen in Fig. 4.8(b).

To explain these results, recall that a basic assumptions justifying our discrete-to-continuum modeling procedure is that the discrete lattice can be embedded in a smooth surface. The small scale oscillations we see in Fig. 4.8(b) suggest that this assumption is violated. As a consequence, we do not expect to get a good match between the predictions of the two models. The results in Fig. 4.7 suggest that sufficiently large elastic constants can suppress these small scale oscillations, in which case a good match between the discrete and the continuum is attained.

One could conjecture that the problem is with the use of the Kolmogorov–Crespi-z potential. To show that this is not the case, we compare the predictions of the discrete model using the full Kolmogorov–Crespi potential versus the predictions of the Kolmogorov–Crespi-z potential. See Fig. 4.9. Figs. 4.9(a) and 4.9(b) show the predictions of the discrete model using the full Kolmogorov–Crespi potential and relatively large elastic constants. These simulations use the same parameter values as those used for Fig. 4.7. Figs. 4.9(c) and 4.9(d) show the predictions of the discrete model using the full Kolmogorov–Crespi potential and relatively small elastic constants. These simulations use the same parameter values as those used for Fig. 4.8. By comparing Figs. 4.9(a) and 4.9(b) to Figs. 4.7(a) and 4.7(b) and by comparing Figs. 4.9(c) and 4.9(d) to Figs. 4.8(a) and 4.8(b), we see the same predictions from the discrete model if we use the full Kolmogorov–Crespi potential versus the Kolmogorov–Crespi-z potential.

In Fig. 4.10 we show the predictions of the discrete and continuum models for relatively large elastic constants. These simulations use the same parameter values as those used for Fig. 4.7. Note that here we are using the full Kolmogorov–Crespi potential. As expected from the above discussion, we see a good match between the discrete and the continuum.

Table 4.3

Parameter values for additional simulations using KC potential.

(a) Parameters for the discrete model. All lengths are in Å. θ is in degrees. k_s , k_t , k_d , and ω are in eV.									
	h_0 , h	L	θ	k_s	k_t	k_d	σ	ω	δ
Figs. 4.7, 4.9(a),(b), 4.10	2.46	120	-2.03	3.23	0.75	12	3.34	0.01	0.58
Figs. 4.8, 4.9(c),(d)	2.46	120	-2.03	0.403	0.015	1.20	3.34	0.01	0.58

(b) Dimensionless parameters for the continuum model. Θ is in radians.									
	ϵ	δ_0 , δ	k	m	α	Θ	γ_s	γ_t	γ_d
Figs. 4.7, 4.9(a),(b), 4.10	0.028	0.74	2	-1	0	-1.28	123.66	306.64	10.39
Figs. 4.8, 4.9(c),(d)	0.028	0.74	2	-1	0	-1.28	15.46	6.13	1.04

5. Conclusions

We derive a continuum model of a graphene bilayer in which one layer is fixed. We start with a discrete energy containing elastic terms and a weak interaction term. After expanding these terms in a small geometric parameter, we truncate the expansions and approximate sums with integrals to arrive at a continuum energy having a Ginzburg–Landau structure.

To validate our modeling, we perform numerical simulations to compare the predictions of the original discrete model and our continuum model. This comparison shows excellent agreement between the two models if the dimensionless elastics constants that appear in the continuum model are sufficiently large. The continuum model predicts spatial patterns that have been observed for twisted graphene bilayers in other papers (van Wijk et al., 2015, 2014; Nam and Koshino, 2017; Jain et al., 2016; Enaldiev et al., 2020). For the out-of-plane displacement, the model predicts hot spots and wrinkles connecting neighboring hot spots. These wrinkles form domain walls between relatively large triangular commensurate regions.

For certain cases, we see discrepancies between what the discrete and continuum models predict for the out-of-plane displacements of some hot spots and wrinkles. This occurs for both the Lennard-Jones potential and the Kolmogorov–Crespi potential. Surface plots of solutions show small-scale spatial oscillations in the horizontal displacement when the elastic constants are not sufficiently large relative to the strength of the weak interaction. The existence of these oscillations violates a basic assumption of our discrete-to-continuum modeling procedure, and we believe that this explains why the discrepancies occur. For the Lennard-Jones potential, decreasing ω , which controls the strength of the weak interaction, increases the dimensionless elastic constants that appear in the continuum model. In this case, we see a good match for the out-of-plane displacement of all hot spots and wrinkles. Likewise, we see a good match for the Kolmogorov–Crespi potential when we directly increase the size of the elastic constants in the discrete model.

In this paper, we apply our discrete-to-continuum modeling procedure to a discrete energy in which the weak-interaction term is based on either the Lennard-Jones potential or a version of the Kolmogorov–Crespi potential that assumes that the layers are locally parallel. Each of these potentials has the feature that the interaction between two non-bonded atoms is computed from a simple function of the positions of the two atoms. In particular, neither of these potentials requires additional information about the layers near the atoms, for example, information about the local orientation of the normals. Our approach is based on finding the local horizontal offset in the reference configuration. We decompose this offset into contributions from the lattice mismatch of the layers and from the misalignment between the layers. Because of the relatively simple form of the potentials we work with here, we can in a straightforward way incorporate these contributions as parameters in the final form of the potential in the continuum model. It would be of interest to explore whether this approach can be adapted to more complicated potentials. For example, the full Kolmogorov–Crespi potential depends not just on the positions of the interacting atoms but also on the local orientation of the lattices near the atoms.

CRediT authorship contribution statement

Malena I. Español: Conceptualization, Methodology, Formal analysis, Investigation, Writing – original draft, Writing – review & editing, Visualization. **Dmitry Golovaty:** Conceptualization, Methodology, Formal analysis, Investigation, Writing – original draft, Writing – review & editing, Visualization. **J. Patrick Wilber:** Conceptualization, Methodology, Formal analysis, Investigation, Writing – original draft, Writing – review & editing, Visualization.

Declaration of competing interest

The authors declare that they have no known competing financial interests or personal relationships that could have appeared to influence the work reported in this paper.

Data availability

No data was used for the research described in the article.

Acknowledgment

This work was supported by the National Science Foundation, United States grant DMS-1615952.

Appendix A. Supplementary data

Supplementary material related to this article can be found online at <https://doi.org/10.1016/j.jmps.2023.105229>. The supplementary material contains details on the asymptotic expansions used to derive the continuum model.

References

- COMSOL Multiphysics® v. 5.3, COMSOL AB, Stockholm, Sweden, <http://www.comsol.com/>.
- Andrei, E.Y., MacDonald, A.H., 2020. Graphene bilayers with a twist. *Nature Mater.* 19 (12), 1265–1275.
- Braides, A., 2014. Discrete-to-continuum variational methods for lattice systems. In: Proceedings International Congress of Mathematicians. Seoul. pp. 997–1015.
- Braides, A., Solci, M., Vitali, E., 2007. A derivation of linear elastic energies from pair-interaction atomistic systems. *Networks Heterog Media* 2 (3), 551.
- Cao, Y., Fatemi, V., Fang, S., Watanabe, K., Taniguchi, T., Kaxiras, E., Jarillo-Herrero, P., 2018. Unconventional superconductivity in magic-angle graphene superlattices. *Nature* 556 (7699), 43–50.
- Carr, S., Fang, S., Kaxiras, E., 2020. Electronic-structure methods for twisted moiré layers. *Nat. Rev. Mater.* 5 (10), 748–763.
- Carr, S., Fang, S., Zhu, Z., Kaxiras, E., 2019. Exact continuum model for low-energy electronic states of twisted bilayer graphene. *Phys. Rev. Res* 1 (1), 013001.
- Carr, S., Massatt, D., Torrisi, S.B., Cazeaux, P., Luskin, M., Kaxiras, E., 2018. Relaxation and domain formation in incommensurate two-dimensional heterostructures. *Phys. Rev. B* 98 (22), 224102.
- Cazeaux, P., Luskin, M., Massatt, D., 2020. Energy minimization of two dimensional incommensurate heterostructures. *Arch. Ration. Mech. Anal.* 235 (2), 1289–1325.
- Dai, S., Xiang, Y., Srolovitz, D.J., 2016a. Structure and energetics of interlayer dislocations in bilayer graphene. *Phys. Rev. B* 93 (8), 085410.
- Dai, S., Xiang, Y., Srolovitz, D.J., 2016b. Twisted bilayer graphene: Moiré with a twist. *Nano Lett.* 16 (9), 5923–5927.
- Dong, K., Zhang, T., Li, J., Wang, Q., Yang, F., Rho, Y., Wang, D., Grigoropoulos, C.P., Wu, J., Yao, J., 2021. Flat bands in magic-angle bilayer photonic crystals at small twists. *Phys. Rev. Lett.* 126 (22), 223601.
- Enaldiev, V., Zólyomi, V., Yelgel, C., Magorrian, S., Fal'ko, V., 2020. Stacking domains and dislocation networks in marginally twisted bilayers of transition metal dichalcogenides. *Phys. Rev. Lett.* 124 (20), 206101.
- Español, M.I., Golovaty, D., Wilber, J.P., 2017. Discrete-to-continuum modeling of weakly interacting incommensurate chains. *Phys. Rev. E* 96 (3), 033003.
- Español, M.I., Golovaty, D., Wilber, J.P., 2018. Discrete-to-continuum modelling of weakly interacting incommensurate two-dimensional lattices. *Proc. R. Soc. Lond. Ser. A Math. Phys. Eng. Sci.* 474 (2209), 20170612.
- Halbertal, D., Finney, N.R., Sunku, S.S., Kerelsky, A., Rubio-Verdú, C., Shabani, S., Xian, L., Carr, S., Chen, S., Zhang, C., et al., 2021. Moiré metrology of energy landscapes in van der Waals heterostructures. *Nature Commun.* 12 (1), 1–8.
- Jain, S.K., Jurić, V., Barkema, G.T., 2016. Structure of twisted and buckled bilayer graphene. *2D Materials* 4 (1), 015018.
- Kolmogorov, A.N., Crespi, V.H., 2005. Registry-dependent interlayer potential for graphitic systems. *Phys. Rev. B* 71, 235415. <http://dx.doi.org/10.1103/PhysRevB.71.235415>.
- Li, T., Jiang, S., Li, L., Zhang, Y., Kang, K., Zhu, J., Watanabe, K., Taniguchi, T., Chowdhury, D., Fu, L., et al., 2021. Continuous mott transition in semiconductor moiré superlattices. *Nature* 597 (7876), 350–354.
- Nam, N.N.T., Koshino, M., 2017. Lattice relaxation and energy band modulation in twisted bilayer graphene. *Phys. Rev. B* 96, 075311. <http://dx.doi.org/10.1103/PhysRevB.96.075311>.
- Novoselov, K., Mishchenko, A., Carvalho, A., Neto, A.C., 2016. 2D materials and van der Waals heterostructures. *Science* 353 (6298), aac9439.
- Plimpton, S., 1995. Fast parallel algorithms for short-range molecular dynamics. *J. Comput. Phys.* (ISSN: 0021-9991) 117 (1), 1–19. <http://dx.doi.org/10.1006/jcph.1995.1039>, Available at <http://lammps.sandia.gov>.
- Sulleiro, M.V., Develioğlu, A., Quirós-Ovies, R., Martín-Pérez, L., Sabanés, N.M., González-Juarez, M.L., Gómez, I.J., Vera-Hidalgo, M., Sebastián, V., Santamaría, J., et al., Fabrication of devices featuring covalently linked MoS₂-graphene heterostructures, *Nat. chem.*
- Sunku, S., Ni, G., Jiang, B.-Y., Yoo, H., Sternbach, A., McLeod, A., Stauber, T., Xiong, L., Taniguchi, T., Watanabe, K., et al., 2018. Photonic crystals for nano-light in moiré graphene superlattices. *Science* 362 (6419), 1153–1156.
- Tran, K., Moody, G., Wu, F., Lu, X., Choi, J., Kim, K., Rai, A., Sanchez, D.A., Quan, J., Singh, A., et al., 2019. Evidence for moiré excitons in van der Waals heterostructures. *Nature* 567 (7746), 71–75.
- Vitek, V., 1968. Intrinsic stacking faults in body-centred cubic crystals. *Phil. Mag. A* 18 (154), 773–786. <http://dx.doi.org/10.1080/14786436808227500>.
- Weston, A., Zou, Y., Enaldiev, V., Summerfield, A., Clark, N., Zólyomi, V., Graham, A., Yelgel, C., Magorrian, S., Zhou, M., et al., 2020. Atomic reconstruction in twisted bilayers of transition metal dichalcogenides. *Nature Nanotechnol.* 15 (7), 592–597.
- van Wijk, M.M., Schuring, A., Katsnelson, M.I., Fasolino, A., 2014. Moiré patterns as a probe of interplanar interactions for graphene on h-BN. *Phys. Rev. Lett.* 113 (13), 135504.
- van Wijk, M.M., Schuring, A., Katsnelson, M.I., Fasolino, A., 2015. Relaxation of moiré patterns for slightly misaligned identical lattices: graphene on graphite. *2D Materials* 2 (3), 034010.
- Xiang, R., Inoue, T., Zheng, Y., Kumamoto, A., Qian, Y., Sato, Y., Liu, M., Tang, D., Gokhale, D., Guo, J., et al., 2020. One-dimensional van der Waals heterostructures. *Science* 367 (6477), 537–542.
- Yoo, H., Engelke, R., Carr, S., Fang, S., Zhang, K., Cazeaux, P., Sung, S.H., Hovden, R., Tsai, A.W., Taniguchi, T., et al., 2019. Atomic and electronic reconstruction at the van der Waals interface in twisted bilayer graphene. *Nature Mater.* 18 (5), 448–453.
- Zhang, K., Tadmor, E.B., 2017. Energy and moiré patterns in 2D bilayers in translation and rotation: A study using an efficient discrete–continuum interlayer potential. *Extreme Mech. Lett.* 14, 16–22.
- Zhang, K., Tadmor, E.B., 2018. Structural and electron diffraction scaling of twisted graphene bilayers. *J. Mech. Phys. Solids* 112, 225–238.
- Zhou, S., Han, J., Dai, S., Sun, J., Srolovitz, D.J., 2015. Van der waals bilayer energetics: Generalized stacking-fault energy of graphene, boron nitride, and graphene/boron nitride bilayers. *Phys. Rev. B* 92 (15), 155438.